CHARACTERIZATION OF FRACTURED RESERVOIRS IN ULTRA-DEEP CARBONATE BURIED-HILLS, LANGGU DEPRESSION, CHINA

A Thesis

by

HONGYU TIAN

Submitted to the Office of Graduate and Professional Studies of
Texas A&M University
in partial fulfillment of the requirements for the degree of

MASTER OF SCIENCE

Chair of Committee,	Yuefeng Sun
Committee Members,	Mark E. Everett
	David Schechter
Head of Department,	Michael C. Pope

August 2016

Major Subject: Geology

ABSTRACT

Low-porosity highly fractured carbonate rocks in the deep Ordovician Formation in the Langgu depression of China remain active exploration targets. However, the seismic characterization of fractured reservoirs has been a challenging problem for decades. By integrating logs with seismic data acquired from the Huabei Oilfield in the Langgu depression, we improved a rock-physics-based method of estimating fractured zones using post-stack seismic data combined with stress field analysis. Using an FMI image log, porosity, density as well as sonic logs, fractured zones and heterogeneous rock types are classified. Two reservoir types are identified as having different elastic properties: the high-porosity zone (ϕ>6.5%) and the fractured zone (ϕ<6.5%). Further, by using a pore structure parameter γ from a rock physics model, it has been found that acoustic impedance correlates well with both porosity and this pore structure parameter, for the oil reservoir of the ultra-deep carbonate buried-hill of the Ordovician Age. Fractured zones in the studied reservoirs have a signature of acoustic impedance lower than 16500 (g/cc*m/s) and a pore structure parameter higher than 14. Quantitative geological interpretation further indicates that fractured zones are mostly located along the faults whereas high-porosity zones are distributed along the unconformity surface formed by dominating diagenetic processes.

DEDICATION

I dedicate my thesis to my parents who have given me great support.

ACKNOWLEDGEMENTS

I would like to thank my committee chair, Dr. Yuefeng Sun, and my committee members, Dr. Everett and Dr. Schechter — thanks for their support and guidance with my research and studies. I would also like to thank my group members and other colleagues in Geology and Geophysics Department.

NOMENCLATURE

V_p	Compression Wave Velocity
V_s	Shear Wave Velocity
K	Bulk Modulus
K_s	Solid Bulk Modulus
K_f	Fluid Bulk Modulus
K_d	Dry Bulk Modulus
μ	Shear Modulus
ρ	Bulk Density
ρ_m	Matrix Density
ρ_f	Fluid Density
ρ_w	Water Density
ρ_g	Gas Density
S_w	Water Saturation
S_g	Gas Saturation
V_{sh}	Volume of Shale
$V_{calcite}$	Volume of Calcite
$V_{dolomite}$	Volume of Dolomite
ϕ	Porosity
γ	Frame Flexibility Factor
μ_d	Dry Rock Shear Modulus

U	Photoelectric Cross Section
$U_{calcite}$	Photoelectric Cross Section of Calcite
$U_{dolomite}$	Photoelectric Cross Section of Dolomite
U_{sh}	Photoelectric Cross Section of Shale

TABLE OF CONTENTS

Page

LIST OF FIGURES

Page

LIST OF TABLES

Page

1. INTRODUCTION

Carbonate rocks hold approximately more than half of the hydrocarbon reserves worldwide, and contain 60 percent oil reserves and 40 percent gas reserves. They deposit in a shallow water environment along slopes, platforms and shelf margins. Carbonate rocks have unique characteristics, including deposition and diagenesis, due to their extremely complex pore system. Their petrophysical properties (porosity and permeability) are highly dependent on the rock properties (e.g. grain composition, grain size or skeletal morphology), diagenetic episodes, and fracture patterns. Rock physics analysis, as a bridge in connecting geology, geophysics, and petroleum engineering, establishes the relationship between rock properties and seismic response. It ties the seismic inversion to the geological interpretation. Pore structure is one of the important factors affecting the seismic velocity in carbonate reservoirs. Therefore, understanding the pore type quantification such as moldic, vuggy, interparticle, intraparticle and fractures plays an important role in carbonate reservoirs. In addition, implementing an accurate rock physics model can address the pore structure effect on seismic wave propagation.

Sun (2000, 2004) defined a frame flexibility factor (γ) to quantify the effect of pore structures on seismic wave velocity in carbonate reservoirs. This has already been successfully applied in several carbonate reservoirs such as the Permian Basin (Dou et al., 2011). In this thesis, Sun's model integrated with post-stack inversion will be applied to a seismic dataset acquired from the Langgu Depression, the Jizhong Subbasin, and the Bohai Bay Basin, in China, in order to detect fractured zones and predict high porosity zones.

1.1 Geological Background

The Bohai Bay Basin is a petroliferous onshore continental fault-bounded basin in northeast China. There are two types of carbonate reservoirs in the Bohai Bay Basin: buried-hill reservoirs and bioclastic limestone reservoirs. Compared with bioclastic limestone reservoirs, buried-hill reservoirs are much thicker and more productive in the Bohai Basin (Chang, 1990). They suffer to long periods of weathering and leaching and by microfractures that trap the oil and gas through an unconformity surface or faults block system dominate them, as shown in Figure 1.3 (Zhai, 1982).

The Jizhong Subbasin is one of the six subbasins in the Bohai Bay Basin and covers approximately 25,000 km^2 (9,700 $mile^2$) of the northern part of China (Zha, 1984). Marine carbonate rocks of buried-hills deposited in the Paleozoic and Proterozoic common develop in the Jizhong Subbasin.

The Langgu Depression is located in the north of the Jizhong Subbasin. It is close to the Wuqing and Xushui Depressions and is bounded by the Niubei slope in the south and the Daxing uplift in the north (Figure 1.1). The Daxing and Niudong-Hexiwu Faults mainly control the development of the Langgu Depression. These two major faults dip in the same direction and run parallel to each other and they extend to the northwest. The dip in the Daxing Fault decreases gradually from high to low, and the Hexiwu Fault is steep all the way down (Liu, 1996).

Hexiwu is a second narrow northwest - southeast structural belt in the eastern part of the Langgu Depression. Fault block systems play an important role in oil and gas exploration in the Langgu Depression. During the Proterozoic and Paleozoic Eras, it was

subject to three dominant tectonic stages including the early-buried stage, the middle uplifted stage, and the late stabilized stage (Yi, 2010). The early stage during the Paleozoic resulted in the hill being buried underwater and having less erosion and undeveloped fractures. The middle uplifted stages created abundant structural fractures during the Mesozoic Era and the late stabilized stages formed reservoir caps around the Cenozoic. The Langgu Depression suffered from these three tectonic stages, which made the primary and secondary porosity in limestone disappear and resulted in strong deformation and a complex fault system. Moreover, the average porosity and permeability were relatively low in the Ordovician Age (Table 1.1). Our study area lies in the northeast of the Hexiwu Belt, which has been subjected to ultra-deep buried (Figure 1.2). According to the research by Guo (2009), the fractures orientation was controlled by the maximum principle stress in the northwest during the Ordovician (Figure 1.4).

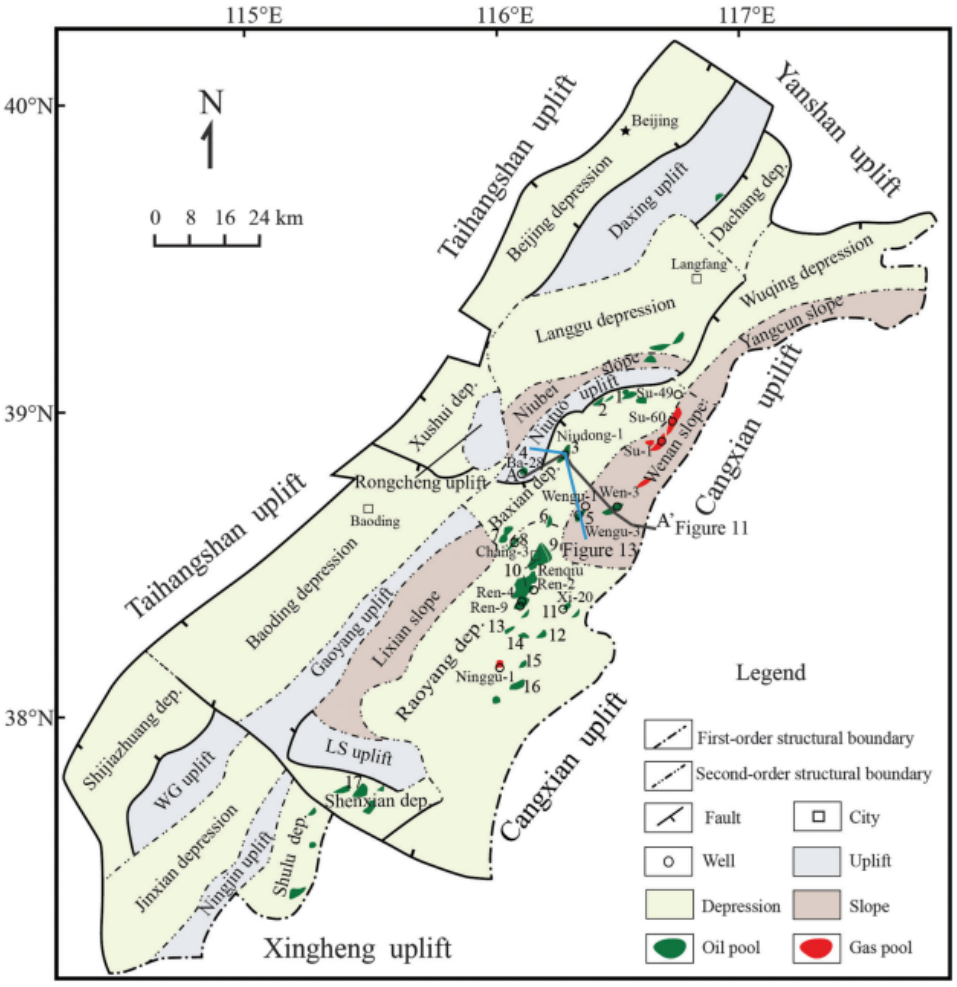

Figure 1.1 Location of Langgu Depression and major structures in the Jizhong Subbasin (Zhao et al., 2015).

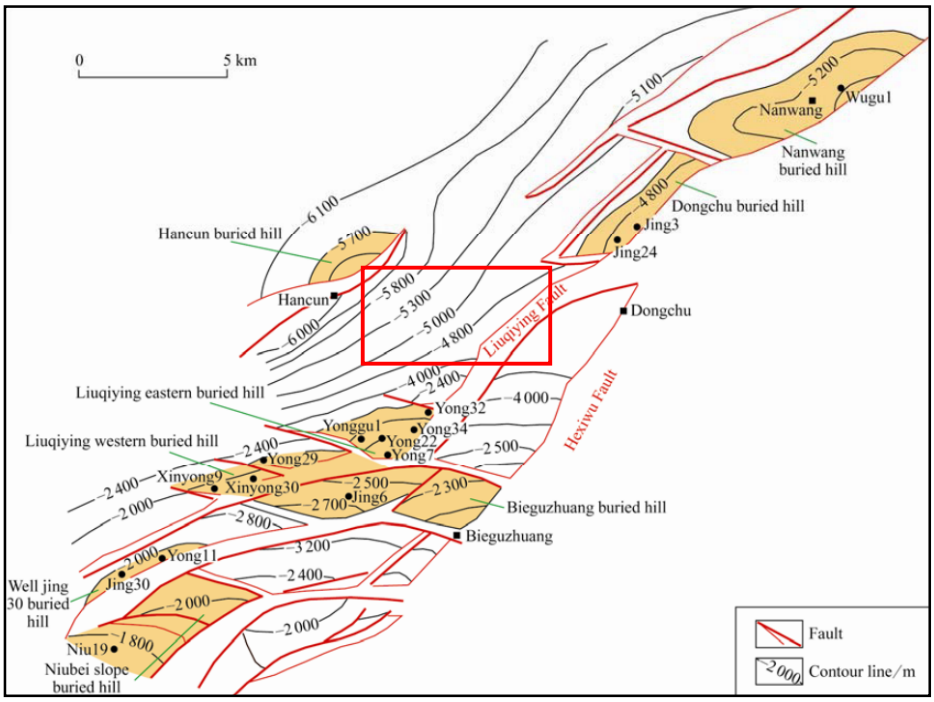

Figure 1.2 Structure top contour map in the Hexiwu area (Guo,2009). The black line shows the structure contour line and the red line represents faults. Our study area is located in the red boxed area.

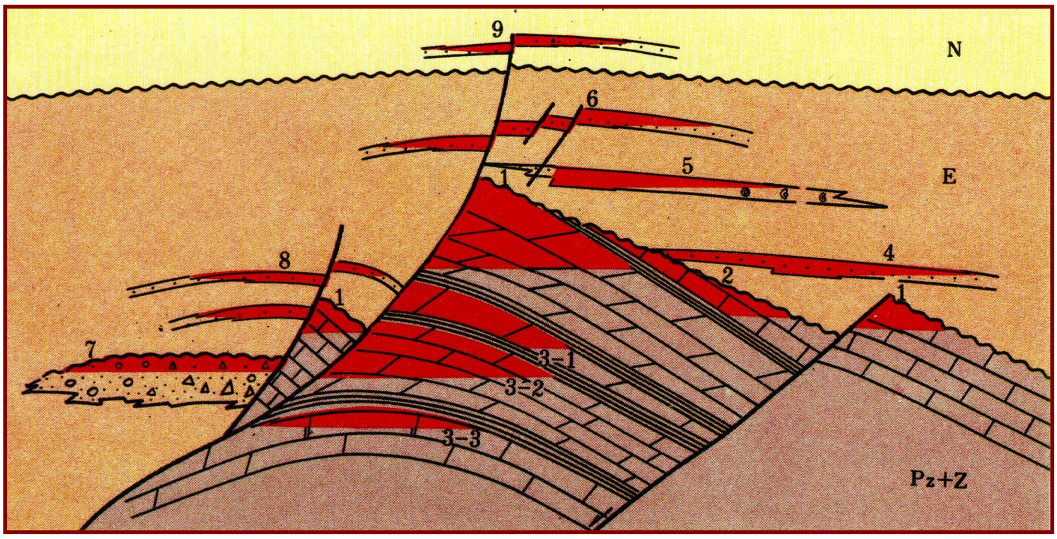

Figure 1.3 Types of hydrocarbon trap and accumulation in the buried-hill (Zhai, 1982). 1: weathering buried-hill top 2: slope of the buried-hill 3: body of the buried-hill trap by the fault system 4: stratigraphic trap of buried-hill 5:biotherm limestone 6&9: fault block system. 7:combination trap 8: rollover structural trap

Table 1.1. The average porosity and permeability in the Langgu Depression modified from Zhao, 2015

Depression	Well	Reservoir interval	Average Porosity (%)	Average Permeability (mD)	Lithology
Langgu	Jing-30	Ordovician	10.7	1.31	limestone
	Yong-22	Ordovician	7	1.15	limestone
	Yong-9	Ordovician	5	0.32	limestone

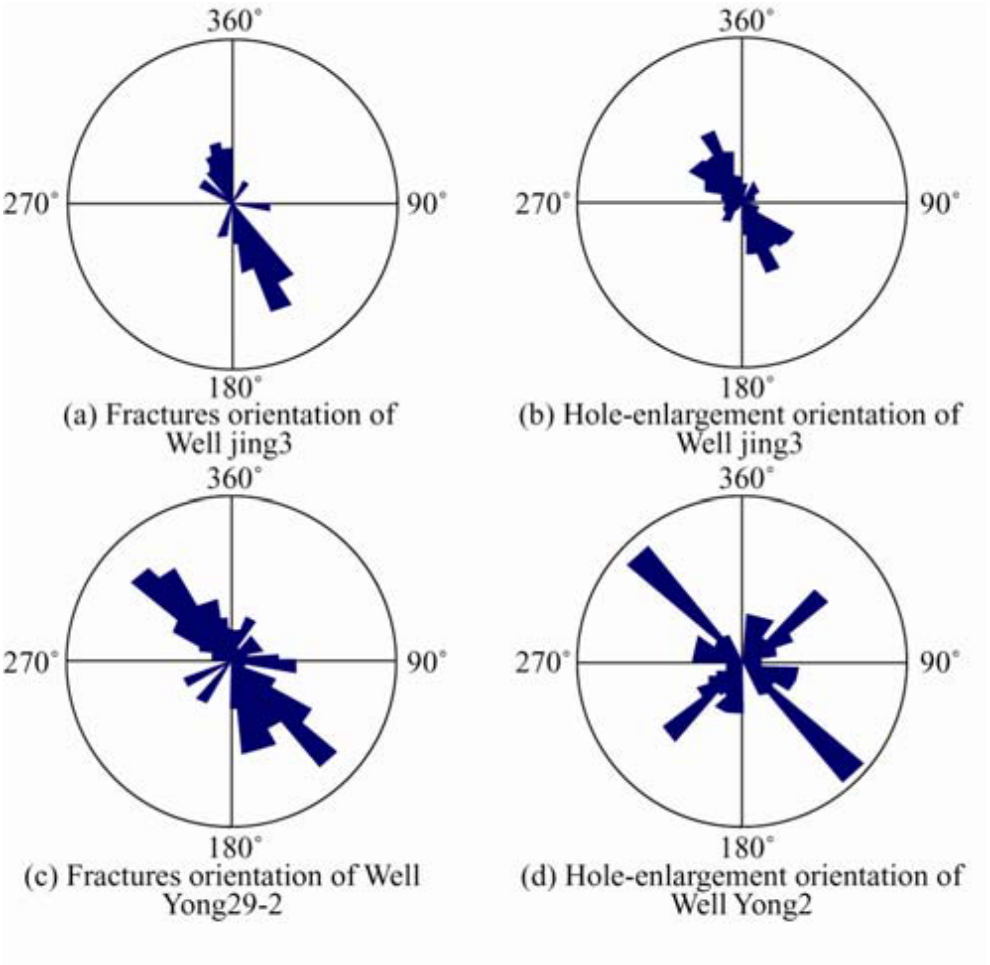

Figure 1.4 Fracture orientation in the Hexiwu area

Ordovician carbonate rocks in the Jizhong Basin are composed of five formations: Fengfeng (O_2f), Shangmajiagou (O_2s), Xiamajiagou (O_2x), Liangjiashan (O_1l), and Yeli (O_1y). Limestone and dolomite were commonly deposited in the Ordovician Period, and mainly produced oil (Figure 1.5). In the Hexiwu area, the top of the Fengfeng Formation is also named as the top of a buried-hill. The Yeli Formation is the bottom for the Ordovician Period in the Jizhong Basin, however, the majority of wells in the Hexiwu area drill completely at the Xiamajiagou Formation so that Xiamajigou is treated as the Ordovician Bottom. Therefore, the target productive reservoirs in the Hexiwu area focus on the Fengfeng, Shangmajiagou and Xiamajiagou Formations.

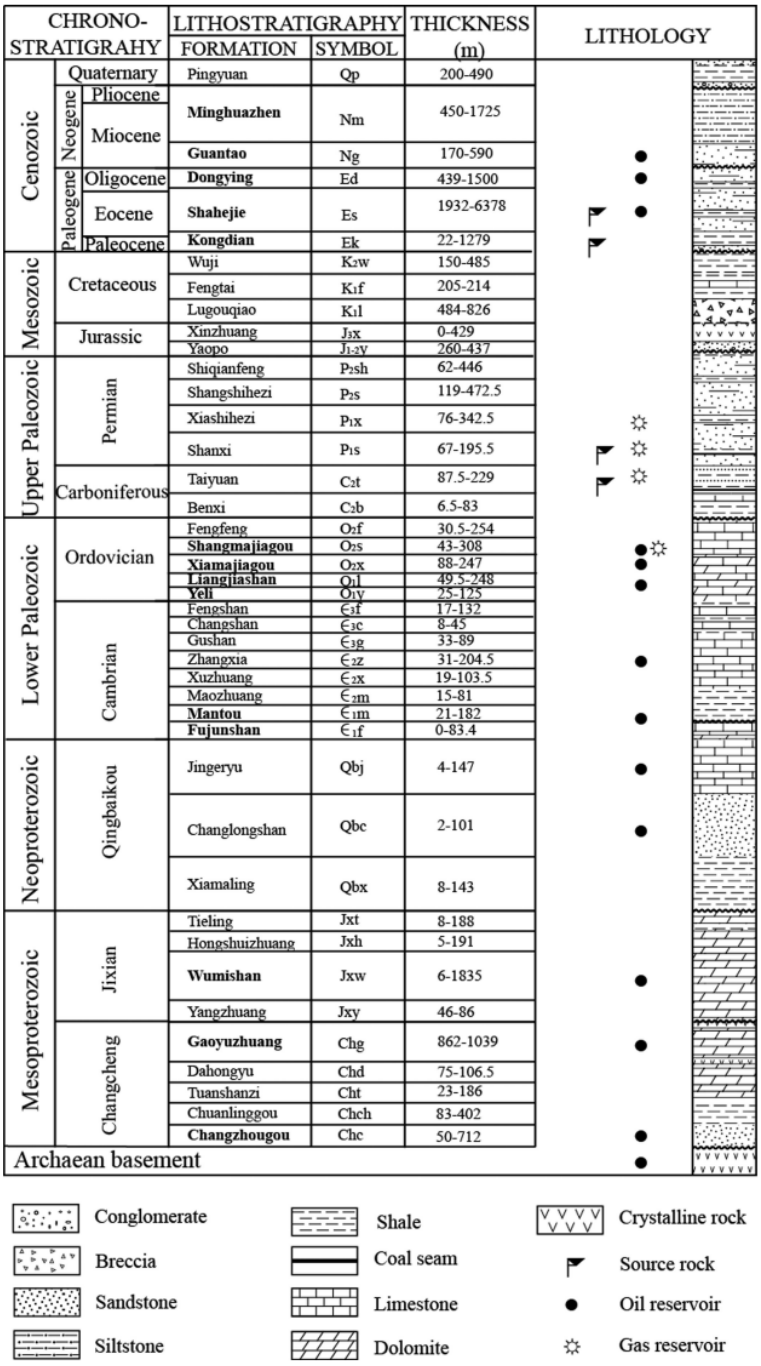

Figure 1.5 The stratigraphy column in the Jizhong Subbasin. (Zhao et al, 2015).

1.2 Well Log and Seismic Datasets

My study area in the Hexiwu area is approximately 182 km^2. The dataset includes a three-dimensional (3-D) post-stack volume and wireline logs from two wells (W2 and W4). The length and the width of the seismic volume are about 12.5 km and 14.5 km respectively. The inline and crossline spacings are both 20 m. The post-stack seismic volume has an average maximum frequency of 60 Hz and an average minimum frequency of 10 Hz. In addition, both of these wells contain the typical well logs, including gamma ray, caliper, density, neutron, compressional and shear wave, deep and shallow resistivity, and PE logs. W4 contains the Full Formation Microimager (FMI) log as well which is used for pore type classification.

1.3 Research Objective

The storage in the Hexiwu carbonate rocks can be identified as dissolution pores, dissolution cavities, and microcracks (Guo, 2009). Fractures play an important role in increasing production from carbonate reservoirs that provide the storage space and fluid flow pathway. Therefore, fracture characterization is a vital part in carbonate reservoir development.

The main objective of this research is to map the distribution of the high porosity and fractured zones in the fault-block system. An integrated rock physics analysis and post-stack seismic inversion method could be used to estimate the occurrence of hydrocarbons in the ultra-deep carbonate buried-hill of the Hexiwu area. The anticipated results are as follows:

(1) The fractured zone and the high porosity zone can be identified from the typical well logs and FMI image logs. They have significant differences in acoustic impedance and bulk modulus distribution. The fractured zone usually has a lower bulk modulus compared with dense limestone at the given porosity.

(2) The high porosity zones are around the top of the buried-hill, and are far away from the faults. The fractured zones are highly developed around the faults in the Shangmajiagou Formation.

By combining regional geology with image-based fracture interpretation, rock physics analysis, and the results of impedance inversion, the distribution of fractured zones will be investigated in relation to the fault-block system and regional tectonic settings.

2. METHODOLOGY

There are several ways to identify fractures on different scales using core samples, thin sections, and electrical image logs. The datasets available for this study did not include any collection of core samples and thin sections. In this thesis, the main emphasis will be to use FMI image logs for fracture identification combined with the analysis of other logs. Fractured zones identified in FMI logs will be separated from high porosity zones using porosity and sonic logs. Then rock physics analysis will be performed using porosity, density, sonic logs, and the results of fracture analysis from FMI logs. The pore-structure parameters that are calculated using the rock physics model will then be used to quantify the fractured zones as well as the high-porosity zones. The correlation of the product of porosity and pore structure parameters with acoustic impedance will be studied for the target formations. Then, the relationship between the two will be used for the post-stack inversion to map the fractured and high porosity zones. Post-stack inversion will be conducted using Jason seismic inversion software.

2.1 Well Log Analysis and Rock Physics Model

Rock physics analysis helps us to understand seismic response and obtain petrophysical properties. The pore type in the buried-hill can be identified from the typical well logs and FMI image logs. Different pore types present different structural features on electrical images as seen from previous research of pore type systems in Ordovician Formation buried-hills. Figure 2.1 illustrates an example of different core scale structures on FMI image log vugs, open fractures, healed fractures, and caves (Zhou et al., 2013).

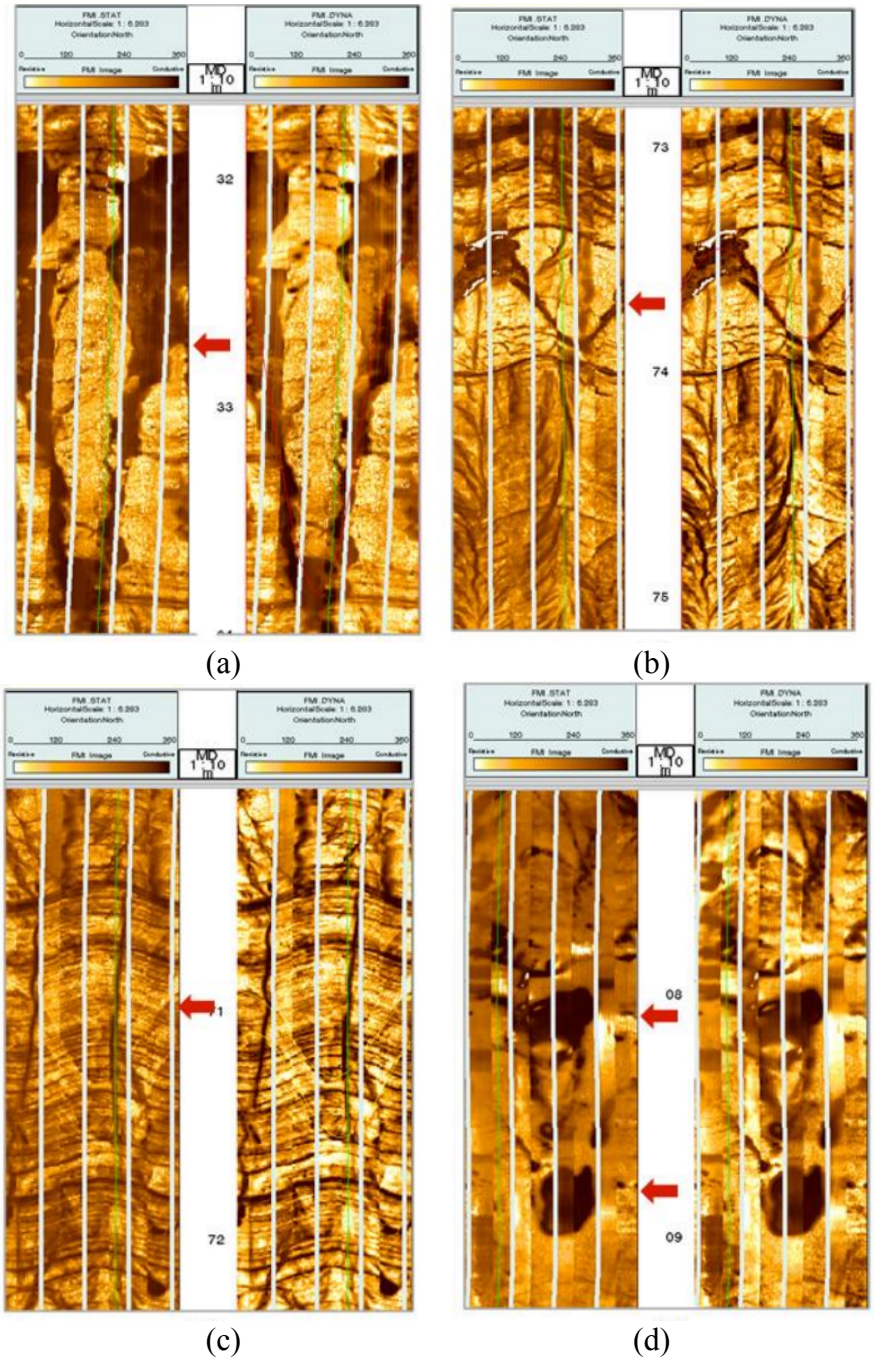

Figure 2.1 FMI images showing different core scale structures on Ordovician Formation buried-hills. (a) solution fracture (b) filled on open fracture (c) healed fracture (d) vugs (e) fault (f) cave. Modified from (Zhou et al., 2013)

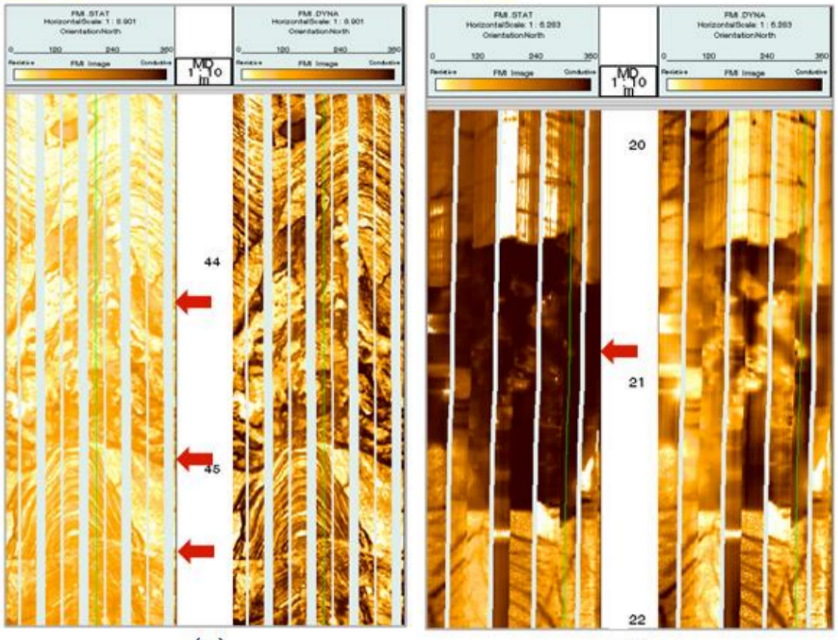

(e) (f)

Figure 2.1 Continued FMI images showing different core scale structures on Ordovician Formation buried-hills. (a) solution fracture (b) filled on open fracture (c) healed fracture (d) vugs (e) fault (f) cave. Modified from (Zhou et al., 2013)

Different pore types display significant features on elastic properties' distribution such as acoustic impedance and bulk modulus. Fractures usually form in the dense and brittle rocks and the fractured zone develops in the low porosity zone compared with the vuggy zones and cavities. In addition to the fractured zone, it has a lower bulk modulus compared with dense limestone at the given porosity. In addition, high porosity zones present a lower bulk modulus and acoustic impedance.

Furthermore, the frame flexibility factor (γ) quantifies the effect of pore structures on the seismic velocity. At the given porosity, the rounder pore structure presents relatively smaller γ values. On the contrary, the narrow pore shaped fractures have larger γ values (Figure 2.2). The cross-plot of density porosity and compressional velocity colored by the pore structure indicate that different pore types affect the compression

velocity classified by the frame flexibility factor (γ) at the same porosity. The fracture has a higher pore structure parameter (γ) while the high porosity has a relativity lower pore structure parameter (γ) (Figure 2.3) (Dou, 2011).

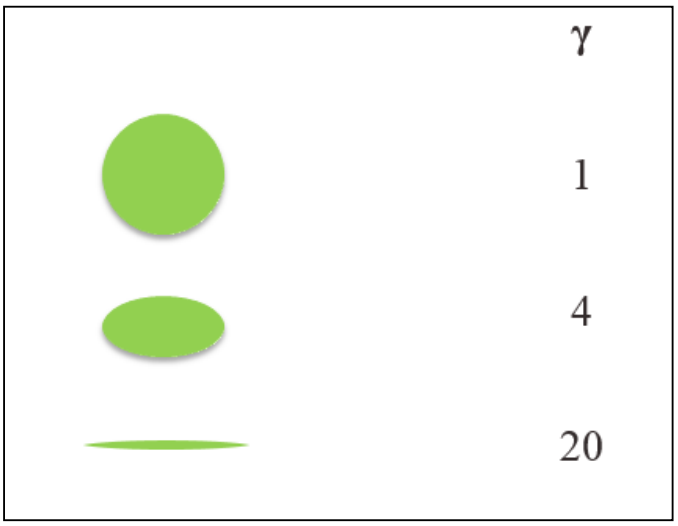

Figure 2.2 Description of frame flexibility factor based on different pore structure at the same porosity.

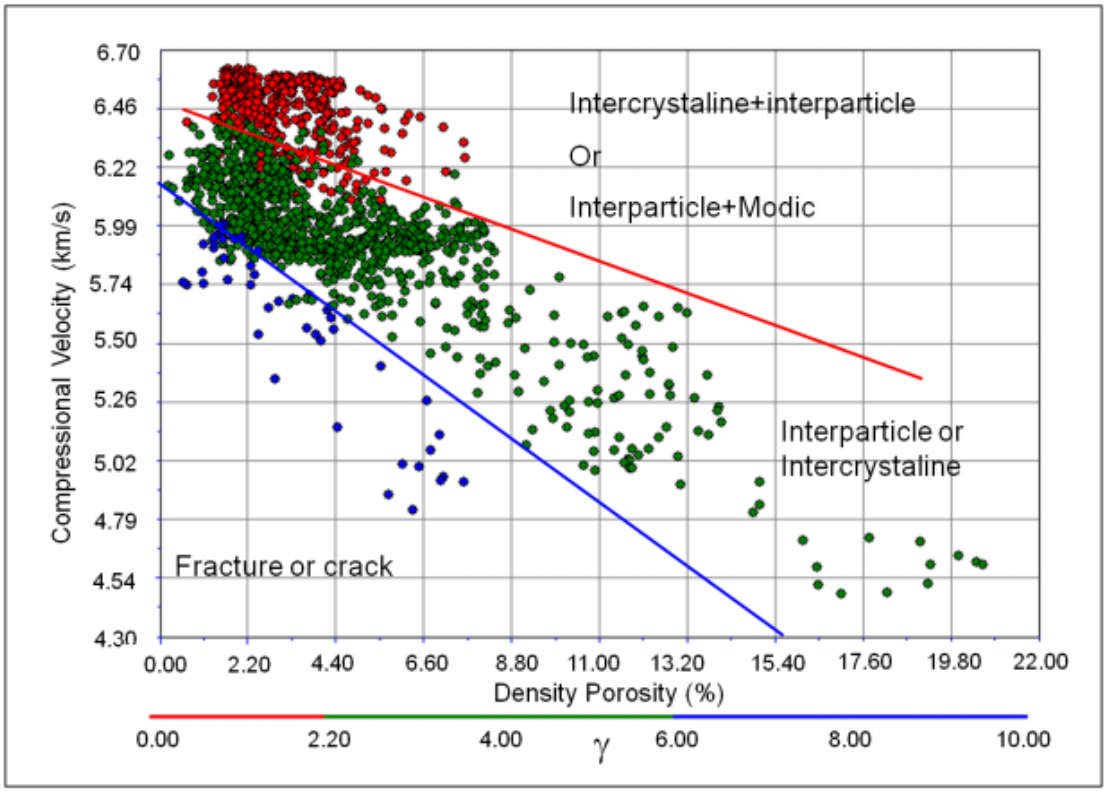

Figure 2.3 Compressional velocity vs. density porosity colored by frame flexibility factor. (Dou, 2011)

This parameter is derived from the equations below:

$$\gamma = 1 + \frac{\ln(f)}{\ln(1-\emptyset)} \tag{2.1}$$

$$f = \frac{1 - (\frac{K_f}{K_s} + (1 - \frac{K_f}{K_s})\emptyset F_k}{(1-\emptyset)(1 - \frac{K_f}{K_s} F_k)} \tag{2.2}$$

$$F_k = \frac{K_s - K}{\emptyset(K_s - K_f)} \tag{2.3}$$

where,

f, γ, F_k: frame flexibility defined in sun's model

K_s: matrix bulk moduli

K_f: fluid bulk moduli

$\emptyset$: density porosity.

Bulk modulus and shear modulus are expressed as:

$$\mathrm{K} = \rho V_p^2 - \frac{4}{3}\mu \tag{2.4}$$

$$\mu = \rho V_s^2 \tag{2.5}$$

Where,

K: bulk moduli

μ: shear moduli

ρ: bulk density measure from density log

V_p: compressional velocity measure from sonic logs

V_s: shear velocity measure from sonic logs.

Density log and DSI (V_p and Vs) logs are used to calculate the bulk and shear moduli from the two equations above. Then equations (2.1)-(2.3) are used to estimate the pore structures from the log-estimated bulk and shear moduli, porosity derived from the density log described below, and the intrinsic matrix and fluid moduli given in Tables 3.1 and 3.2.

The porosity can be estimated from the density log by solving the following equations:

$$\rho_b = \emptyset\rho_f + V_{dolomite}\rho_{dolomite} + V_{calcite}\rho_{calcite} + V_{sh}\rho_{sh} \quad (2.6)$$

$$\rho_m = \rho_{sh}V_{sh} + \rho_{dolomite}V_{dolomite} + \rho_{calcite}V_{calcite} \quad (2.7)$$

$$\mathrm{U} = U_{sh}V_{sh} + U_{dolomite}V_{dolomite} + U_{calcite}V_{calcite} \quad (2.8)$$

$$1 = V_{sh} + V_{dolomite} + V_{calcite} + \emptyset \quad (2.9)$$

Where,

$V_{calcite}$: volume of calcite

$V_{dolomite}$: volume of dolomite

V_{sh}: volume of shale

U: photoelectric cross section

$U_{calcite}$: photoelectric cross section of calcite

$U_{dolomite}$: photoelectric cross section of dolomite

U_{sh}: photoelectric cross section of shale

ρ_b:bulk density measure from density log

ρ_{matrix}: matrix density

$\rho_{calcite}$: density of calcite

$\rho_{dolomite}$: density of dolomite

ρ_{sh}: density of shale

ρ_f: fluid density

And V_{sh}, U, and ρ_f can be estimated by equations (2.10, 2.11 and 2.12)

$$V_{sh} = \frac{GR - GR_{min}}{GR_{max} - GR_{min}} \tag{2.10}$$

$$U = \frac{Pe \times (\rho_b + 0.1883)}{1.0704} \tag{2.11}$$

$$\rho_f = S_w \rho_w + S_g \rho_g \tag{2.12}$$

Where,

GR_{min}: measurement value of gamma ray in pure sand

GR_{max}: measurement value of gamma ray in pure shale

GR: direct gamma tool measurement

Pe: measure from Pe log

S_w: water saturation

S_g: gas saturation

ρ_g: gas density

ρ_w: water density

The relationship between acoustic impedance and reservoir properties in carbonate rocks is very complicated. A new approach improves the linear relationship between acoustic impedance and the product of the porosity and frame flexibility factor, which was used to transform the impedance volume to the porosity volume into seismic inversion (Zhang, 2012). The frame flexibility and porosity volume product can be calculated from constrained sparse spike inversion using, for example, CGG-Jason software.

2.2 Constrained Sparse Spike Inversion

Constrained Sparse spike inversion is one of the deterministic seismic inversion and recursive inversions based on sparse spike deconvolution. It assumes that the sequence of the reflection coefficient extracted from wave impedance is sparse distribution. In other words, the reflection coefficient is composed of a series of major sequence superpositions in a Gaussian background. This inversion uses the minimum reflection coefficient spike to minimize the difference between synthetic trace and original seismic trace, which is constrained with the trend of impedance.

In addition, constrained sparse spike inversion has three significant processes. First, the sparse reflection coefficient is derived by maximum likelihood deconvolution. This target function (Russell, 1988) is,

$$J = \frac{1}{r^2}\sum_{j=1}^{L} r^2(j) + \frac{1}{n^2}\sum_{j=1}^{L} n^2(j) - 2Mln(\lambda) - 2(L-M)\ln(1-\lambda) \quad (2.13)$$

where,

R (j): reflection coefficient in the number of j samples

R: reflection coefficient of strata

M: the reflected number of strata

L: sampling number

N: square root of noise

λ: likelihood value of given reflection coefficient.

Second, the wide band impedance is determined by the maximum likelihood inversion. The equation is shown below (equation 2.14):

$$Z(j) = Z(j-1)\frac{1+R(j)}{1-R(j)} \tag{2.14}$$

Where,

$Z(j)$: impedance

$R(j)$: reflection coefficient.

Third, since the seismic data lacks the low-frequency information and sparse spike inversion acted in the seismic frequency band, we have to compensate the low- frequency information with a well logs curve. A low pass filter is used to filter the logs and is a necessary procedure to obtain the absolute impedance. Hence, the absolute impedance is derived from the trace merge and the low frequency compensation.

Compared with constrained sparse spike inversion, the geostatistic inversion needs more wells to be accurate since the study area has limited wells. Thus, the constrained sparse spike inversion is used in the future study.

3. WELL LOGS ANALYSIS AND ROCK PHYSICS MODELING

The dominant lithology at the buried hill carbonate reservoir in the Langgu Depression consists of limestone and dolomitic limestone. High porosity zones and fractured zones are identified using FMI image logs and typical well logs such as gamma ray, caliper, density, neutron porosity, sonic (compressional velocity and shear velocity), resistivity, and a PE log. Furthermore, the acoustic signature of those zones is identified from the velocity logs, and the rock physics model is built based on the well logs and elastic properties' analysis of W2 and W4.

3.1 Well Logs Analysis in W2 and W4

W4 has two separate well log datasets: typical well logs and FMI image logs. The tools recording the gamma ray log are used to correlate the depth shift. When comparing GR and GR_ETDC, (Figure 3.1) a variation of 3.3 meters can be observed After the depth shift, it is much better to separate the high porosity zone from the dense limestone zone (Figure 3.2).

Poor wellbore quality in W4 causes the caliper log to vary since the weak formations break out and mud cake builds in the permeable zone. The pore space makes the rock conductive whereas rock matrix is non-conductive. The deep burial depth makes the rock dense and the resistivity value extremely high in the Ordovician Formation so that a resistivity log is not a good indicator of the hydrocarbon zone.

According to FMI image logs, the Shangmajiagou Formation is much denser than the Fengfeng and Xiamajiagou Formations. Fractures mainly develop on the bottom of the

Shangmajiagou Formation. Three common pore types in W4 can be identified from FMI image analysis; high porosity (vuggy pores or cavities), fractures, and dense limestone (Figure 3.4). A high porosity zone (Figure 3.4-a) distributes in the Fengfeng formation along the unconformity surface of the buried-hill. The majority of the Ordovician Formation is dense limestone with a few fractures (Figure 3.4-b). Low angle fractures as the dominated fractures in W4 distribute along the bottom of the Shangmajiagou Formation and the top of the Xiamajiagou Formation.

The fractured zone interpreted by the FMI image logs also corresponds with typical well log interpretation (Figure 3.4 and Figure 3.5). At the same porosity, fracture will make the velocity decrease. In addition, when the gamma rays meet the permeable zone, the groundwater will dissolve the uranium and make the gamma value increase. In Figure 3.5, KTH represents the natural gamma radioactivity log without uranium. The standard gamma ray increases at both fractured zones and high porosity zones while the KTH remains constant.

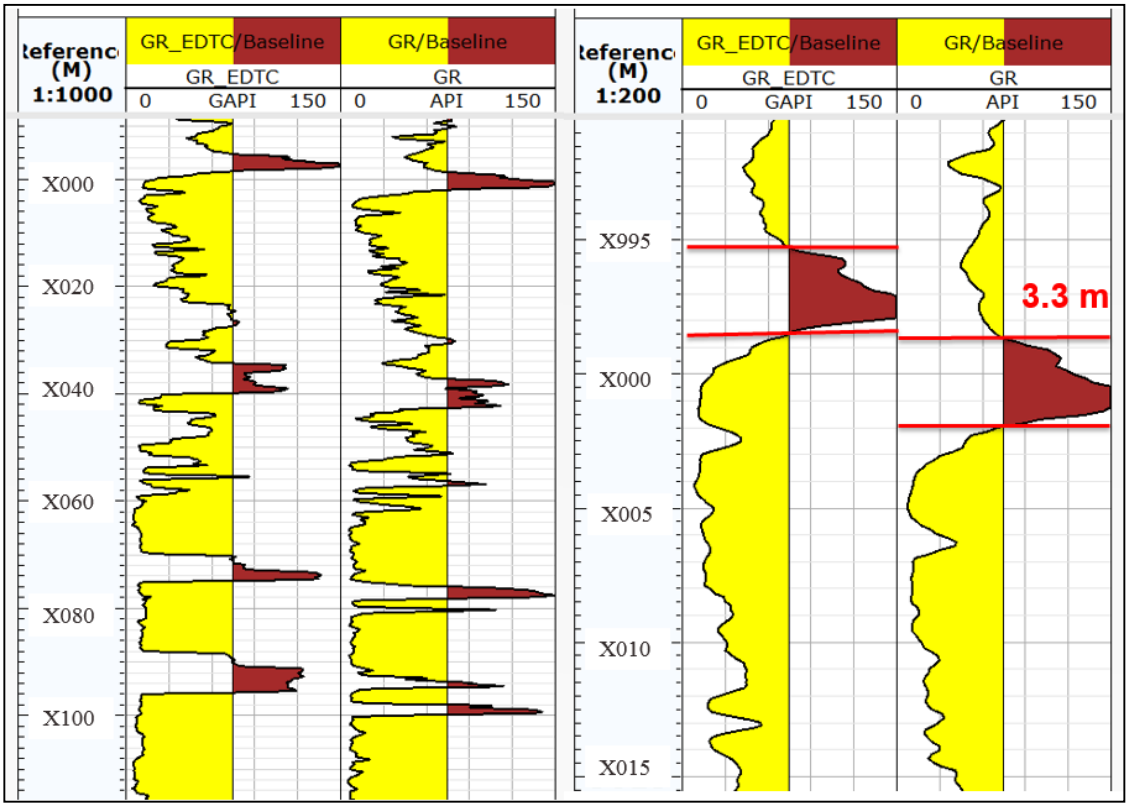

(a) (b)

Figure 3.1 Depth correlation by GR logs in two different datasets. GR_EDTC is from FMI image logs. GR is from typical well logs. Data collected from W4. (a) large scale from depth X900 m to X115 m (b) zoom in scale from depth X991m to X015 m.

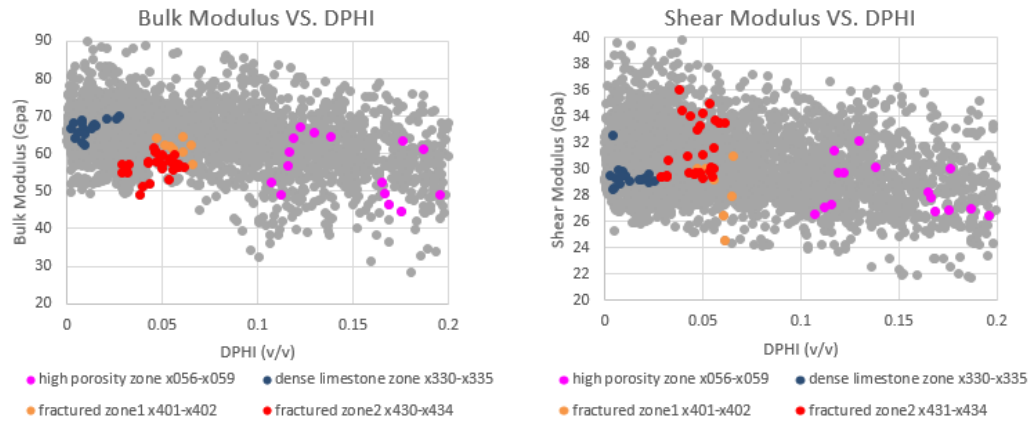

(a)

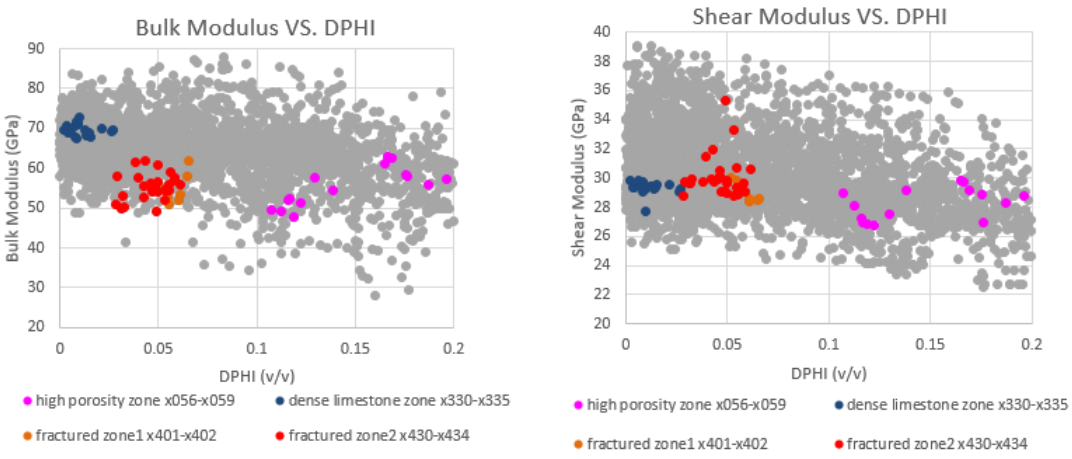

(b)

Figure 3.2 Comparison using crossplot of bulk modulus and porosity and shear modulus and porosity between the depth shift (a) crossplots of bulk/shear modulus and DPHI before depth shift (b) crossplots of bulk/shear modulus and DPHI after depth shift.

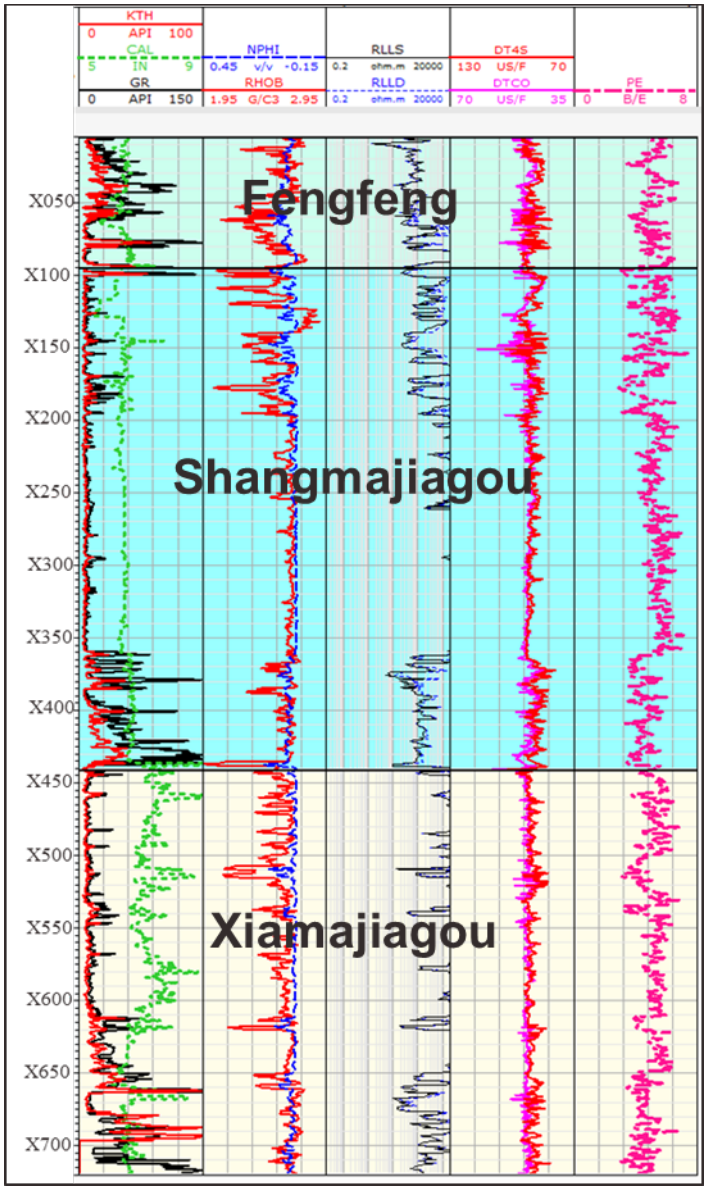

Figure 3.3 Full section view well log curves of W4, Ordovician Formation.

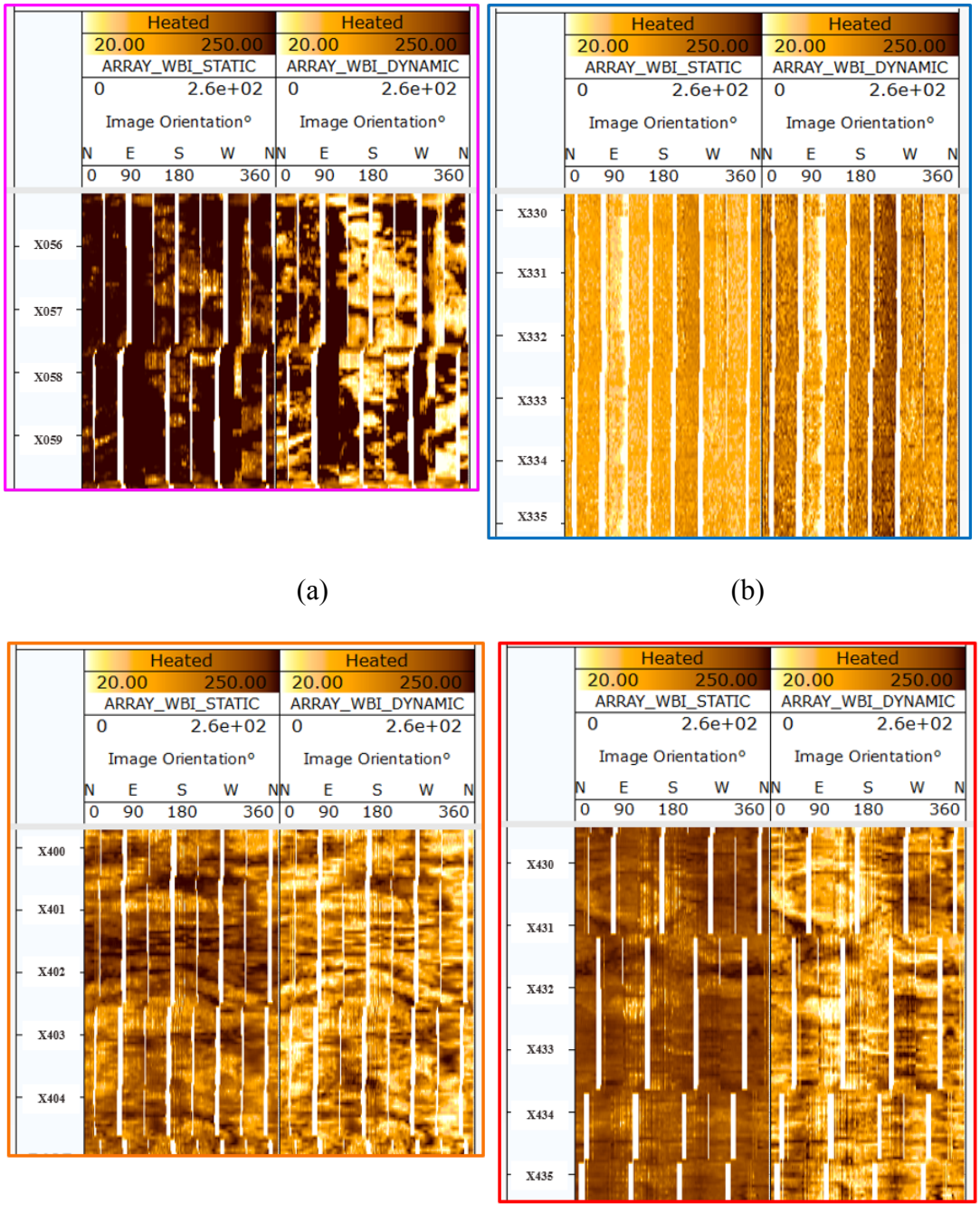

Figure 3.4 FMI image logs showing in W4 (a) high porosity zone (solution pores or cavities) (b) dense limestone zone (c) fractured zone 1 (d) fractured zone 2. Data collected from W4.

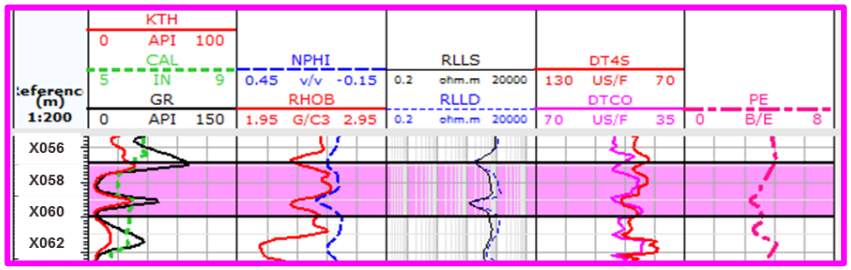

(a)

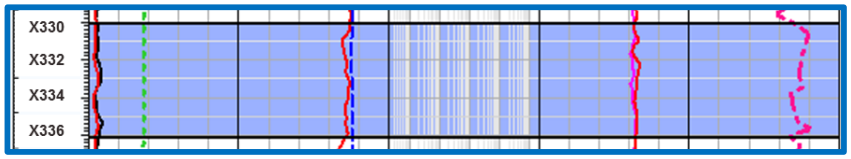

(b)

(c)

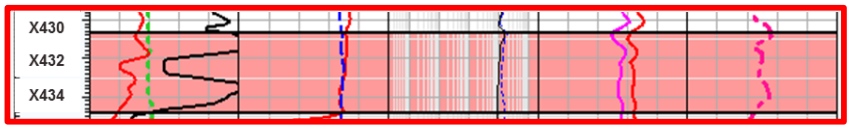

(d)

Figure 3.5 Zoom-in scale section view (a) high porosity zone (b) dense limestone zone (c) fractured zone 1 (d) fractured zone 2. Data collected from W4.

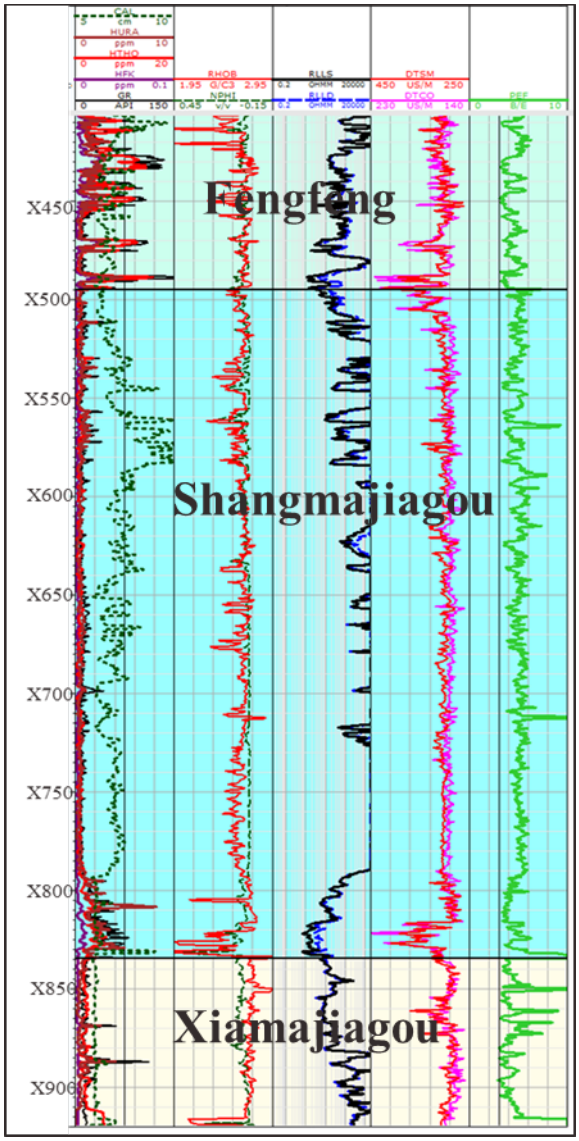

Figure 3.6 Full view well log curves in W2 , Ordovician Formation.

W2 also has poor borehole quality. It is mainly composed of limestone and dolomitic limestone. The pore space developed causes density and sonic log variations at the top of the Fengfeng Formation and the bottom of the Shangmajiagou Formation. The Shangmajiagou Formation is much denser compared with the Fengfeng and Xiamajiagou Formations.

Figure 3.7 illustrates four featured pore types characterized from FMI image logs at W2. Zone a and zone d are interpreted as conductive (healed) fractures and high angle conductive fractures (open fracture). Zone b has higher porosity in typical well log calculations. However, the interpretation from the FMI image logs might be caused by the induced fracture, which is not reliable in the high porosity zone interpretation. Zone c is the dense limestone interval. Fractured zones identified from FMI image logs also correspond with the interpretation in typical well logs. In zone a, because the fracture is filled, the caliper log and density log remain constant. In zone d, the caliper log indicates the break out effect, and density and sonic log curves decrease while the gamma ray increases (Figure 3.8).

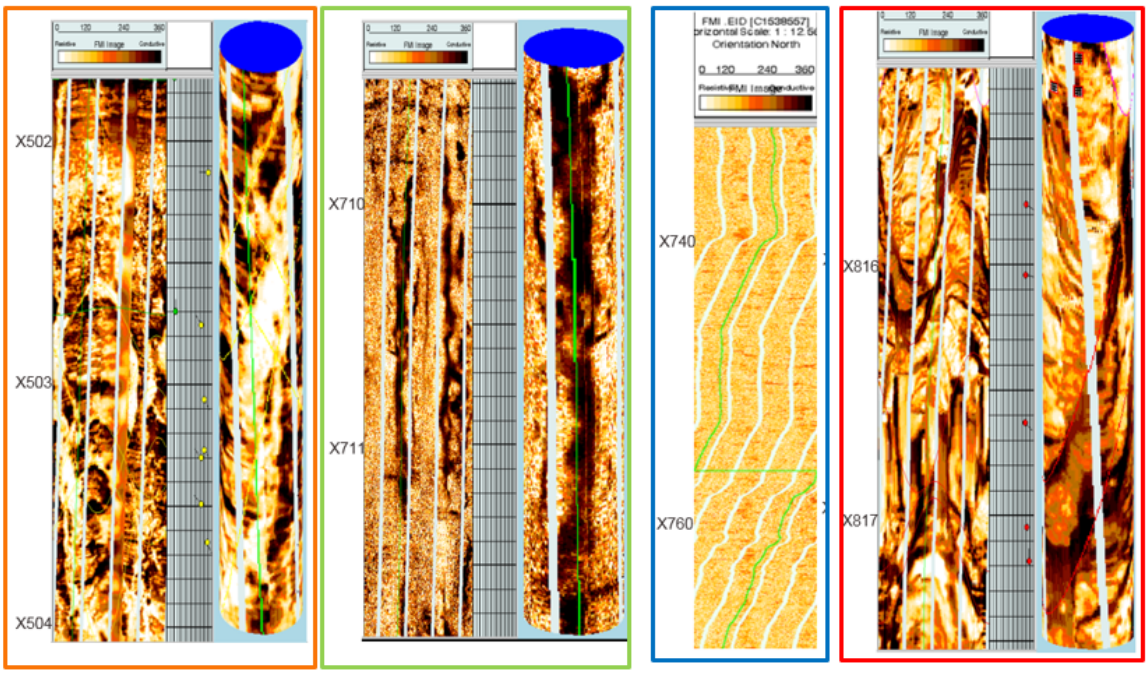

(a) (b) (c) (d)

Figure 3.7 Electrical images from FMI showing (a) fractured zone 1 (b) break out induced fracture (c) dense limestone zone (d) fractured zone 2. Data collected from W2 and provided by the PetroChina Huabei Oilfield.

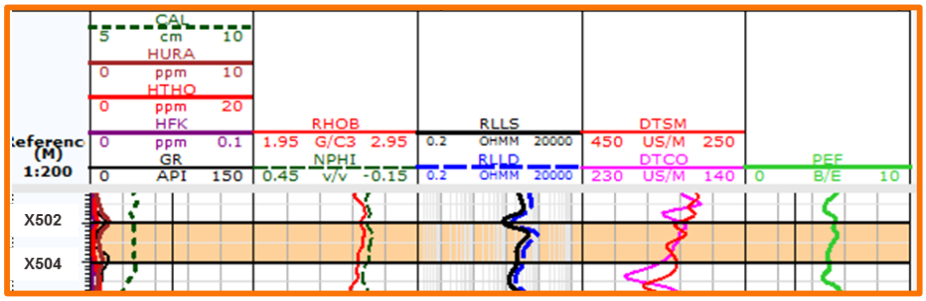

(a)

(b)

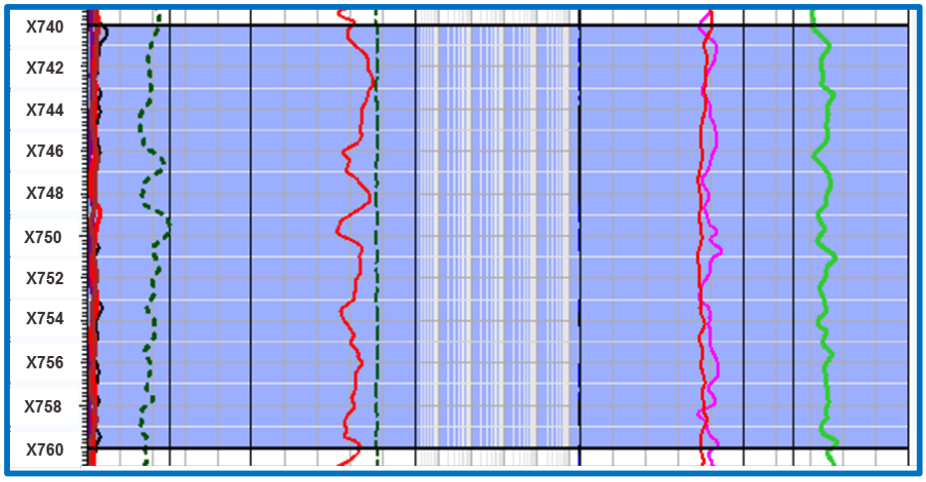

(c)

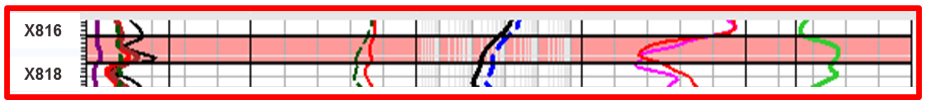

(d)

Figure 3.8 Zoom-in scale correlates with a-d of FMI image log (a) fractured zone 1 (b) induced fracture zone (c) dense limestone zone (d) fractured zone 2.

3.2 Rock Physics Modeling

The main reservoir type can be identified from the W2 and W4 well logs; high porosity such as cave or solution pores and fractures. Integrating rock physics analysis, the fractured zone, and the high porosity zone presents different distributions of elastic properties such as bulk modulus, shear modulus, and acoustic impedance. Different pore types present differently on elastic properties by using the crossplots of bulk modulus or shear modulus versus density porosity (DPHI) and the crossplots of acoustic impedance versus density porosity (DPHI). Figure 3.9 illustrates that the fractured zone has a lower bulk modulus compared with the dense limestone at the given porosity. The high porosity zone interpreted from W4 has a lower bulk modulus and the density porosity is higher than 6.5% (Figure 3.9-b). Both fractured zones interpreted from W2 and W4 show that the porosity is less than 6.5% and the bulk modulus is lower than 60 GPa.

In the acoustic impedance and density porosity crossplots, both fractured zones and high porosity zones have relatively low impedance. Moreover, the high porosity zone has a much lower acoustic impedance than that of the fractured zones. The acoustic impedance of the fractured zone for W2 and W4 is almost less than 15000 g/cc*m/s and 16500g/cc*m/s. W4 has a higher acoustic impedance than that of W2. However, the dense limestone in both wells is higher than 16500 g/cc*m/s, therefore, reservoirs can be identified using a P-impedance cut off of less than 16500 g/cc*m/s (Figure 3.10).

The pore structure parameter (γ) is used to identify the high porosity zone and the fractured zone. The crossplot of bulk modulus versus density porosity colored by the

pore parameter indicates that a pore structure equal to 14 is the boundary between the fractured and the high porosity zones (Figure 3.11).

The product of porosity and pore structure has a better linear relationship with acoustic impedance (Zhang, 2014). Using the crossplot in Figure 3.12 establishes the relationship with acoustic impedance: $\mathrm{AI} = 19000 - 7000(\emptyset \times \gamma)$.

Table 3.1 Parameters used for calculation of density porosity.

Material	Density (g/cc)	U (barns/cm^3)
Calcite	2.71	13.8
Dolomite	2.87	9
Shale	2.64	8.5

Table 3.2 Elastic properties used for calculation of the frame flexibility factor.

Elastic properties	Value (Gpa)
$\boldsymbol{K_s}$	86
$\boldsymbol{K_f}$	2.25
$\boldsymbol{\mu_s}$	41

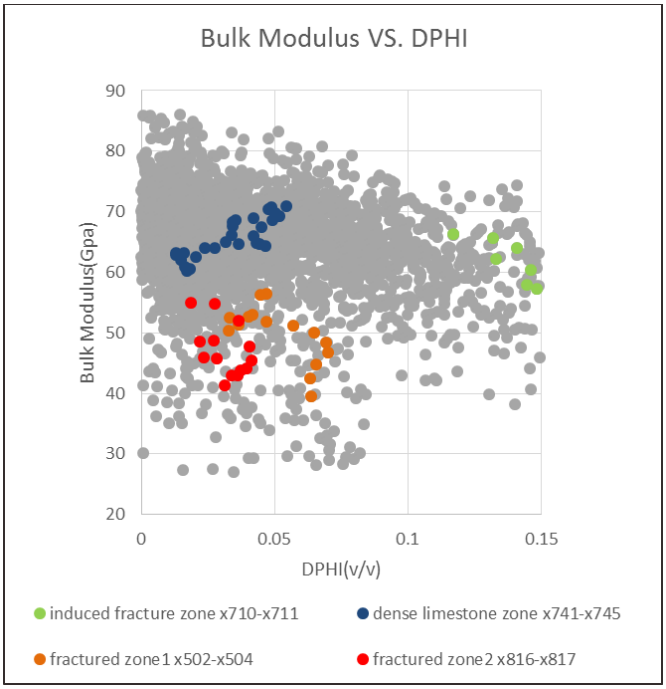

(a)

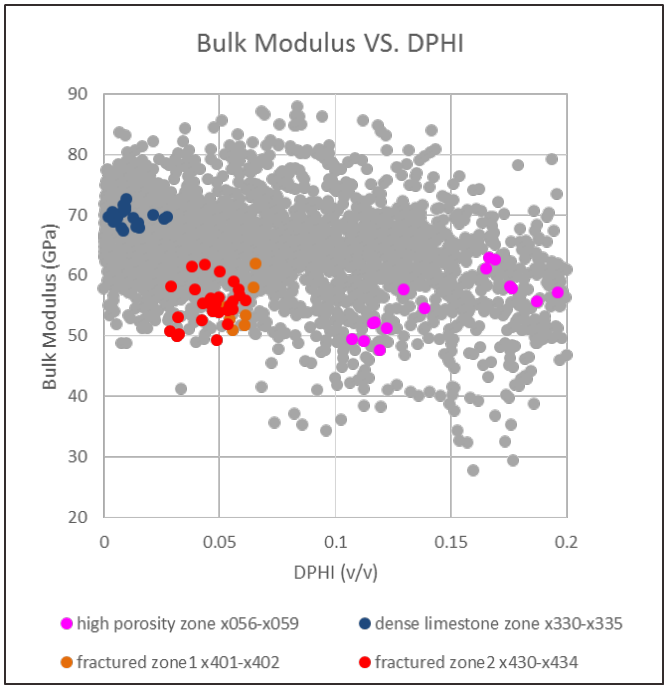

(b)

Figure 3.9 Crossplots of bulk modulus versus porosity on (a) W2 (b) W4.

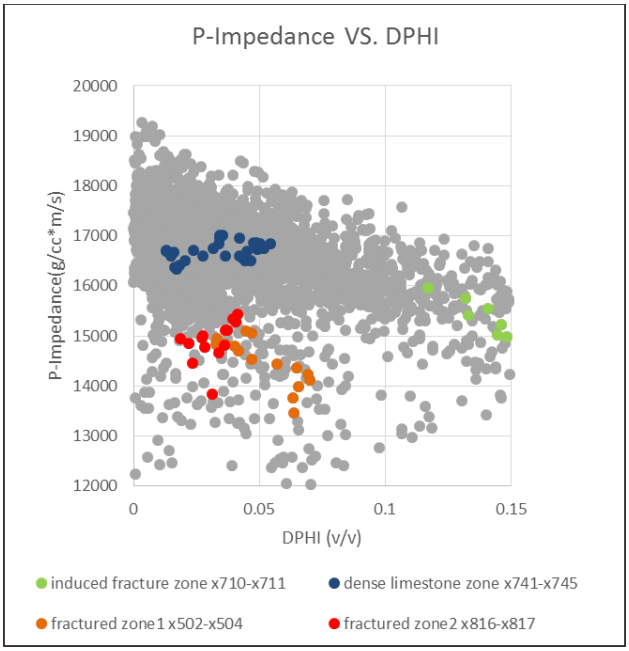

(a)

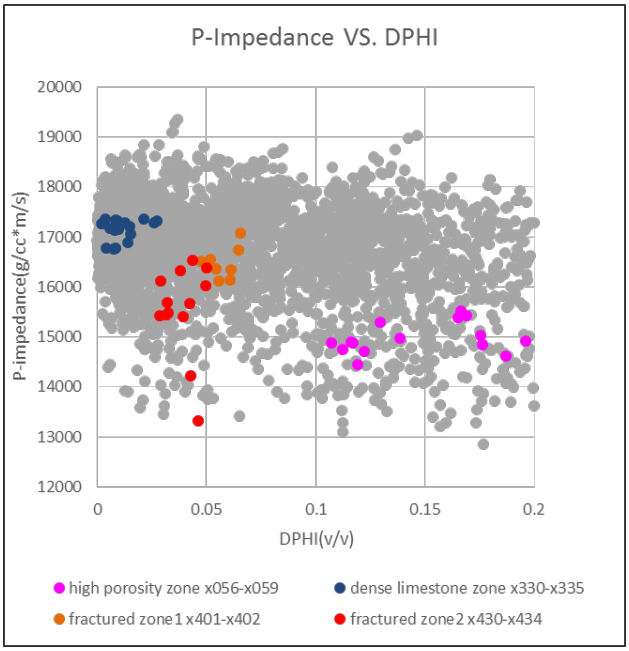

(b)

Figure 3.10 Crossplots of P-impedance versus porosity on (a) W2 (b) W4.

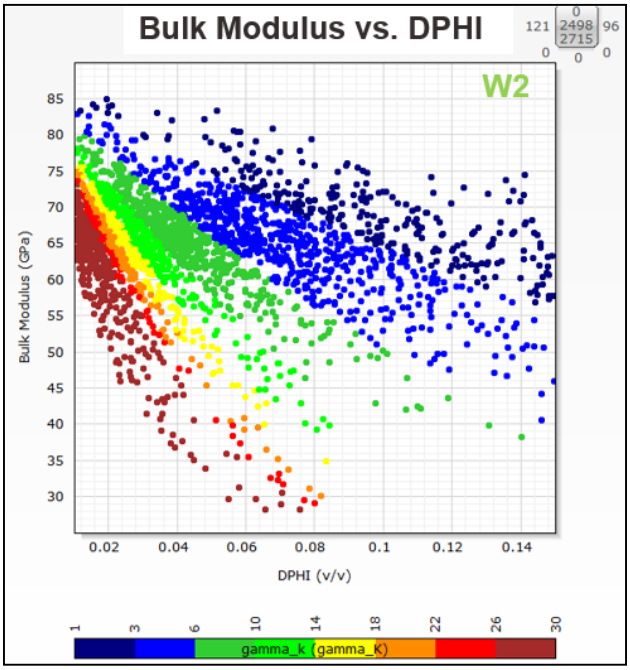

(a)

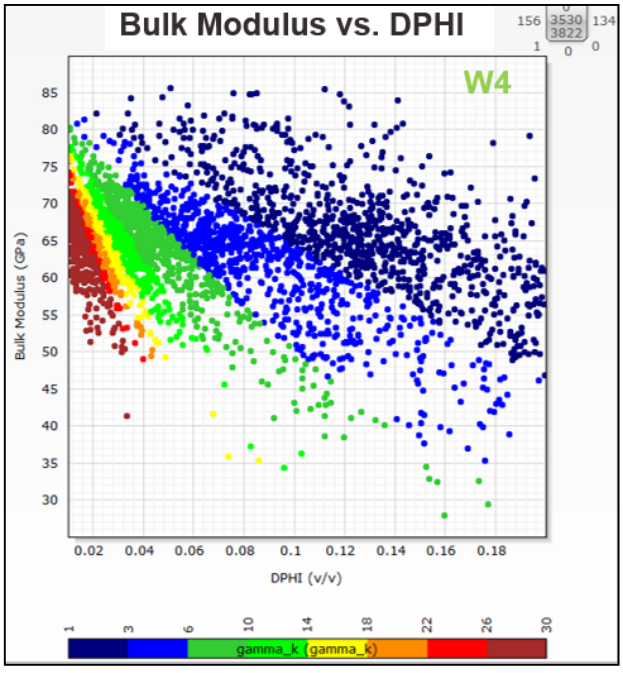

(b)

Figure 3.11 Crossplots of bulk modulus and density porosity (a) W2 (b) W4.

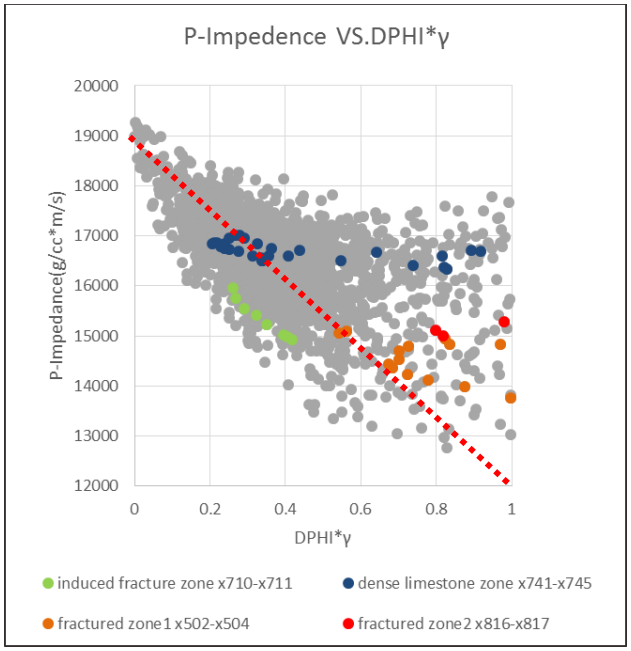

(a)

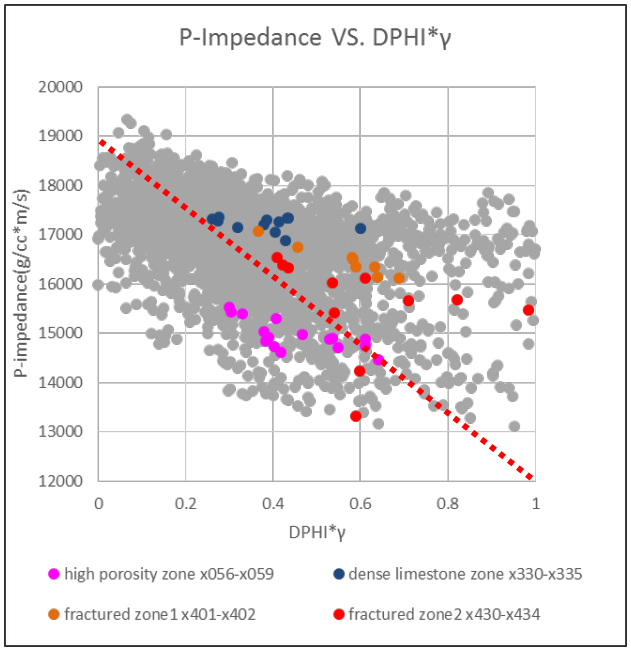

(b)

Figure 3.12 Crossplots of P-Impedance and the product of density porosity and γ in (a) W2 (b) W4.

3.3 Conclusion

From the overall analysis, two reservoir types can be identified from two wells with well log analysis: high-porosity zones (ϕ>6.5%) and fractured zones (ϕ<6.5%) (Figure 3.9, Figure 3.11, and Figure 3.12). The fractured zones in the studied reservoirs have an acoustic impedance of lower than 16500 (g/cc*m/s) and pore structure parameters higher than 14. According to the results of the rock physics analysis, the impedance volume will be obtained from seismic inversion and will be transformed into the porosity product and the frame flexibility factor volume. Usually, the high porosity zone and fractured zone show a high porosity product and frame flexibility factor.

4. POST-STACK SEISMIC INVERSION RESULTS ANALYSIS

Post-stack inversion is generated from InverTrace in Jason. The framework in the low-frequency trend model was built based on horizons. Three horizons from high-resolution (60 Hz) seismic data are interpreted: the top of Fengfeng (Qianshan), the bottom of Shangmajiagou and the bottom of Xiamajiagou (the bottom of Ordovician) (Figure 4.1). According to the map views of the three interpreted horizons, W4 is located much closer to the faults than W2 (Figure 4.2, Figure 4.3, and Figure 4.4). Since the carbonate rocks of Ordovician period deposit in the deep marine environment, these three layers deposit parallel to each other. However, the Hexiwu area suffered long-term tectonic activities resulting in a complex fault-block system. It has five major faults interpreted in the study area and abundant minor faults without interpretation. In Figure 4.5 (Li, 2014), the seismic attributes on the most positive curvature demonstrate that the minor faults are highly developed in this area.

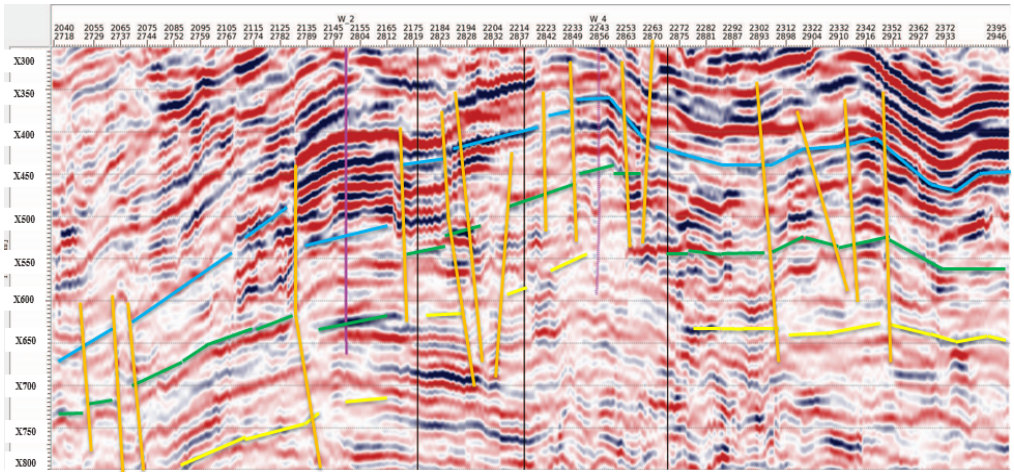

Figure 4.1 Three horizons interpreted on the 60 HZ seismic section view across W2 and W4 in red/ white/black scale. The blue horizon is the top of Fengfeng (Qianshan), the green horizon represents the bottom of Shangmajigou, and the yellow horizon is the bottom of Ordovician.

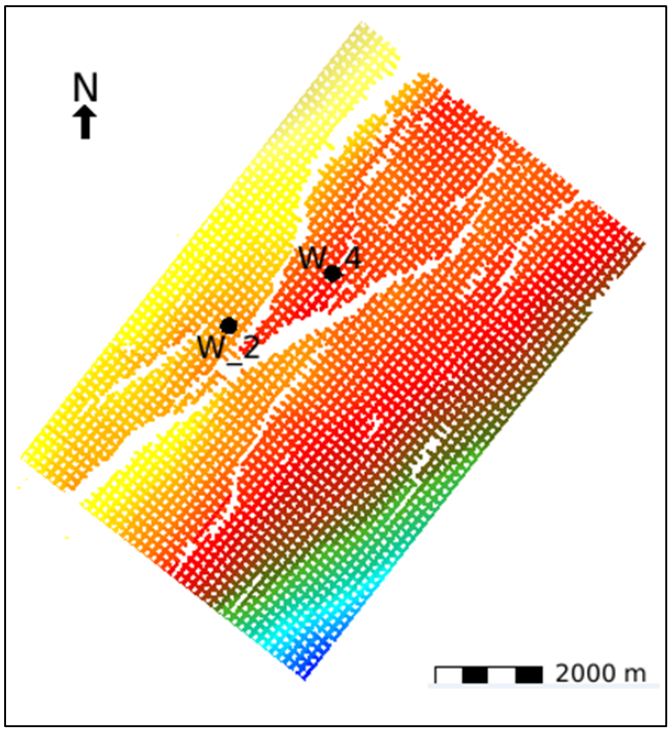

Figure 4.2 Map view for the top of Fengfeng (Qianshan).

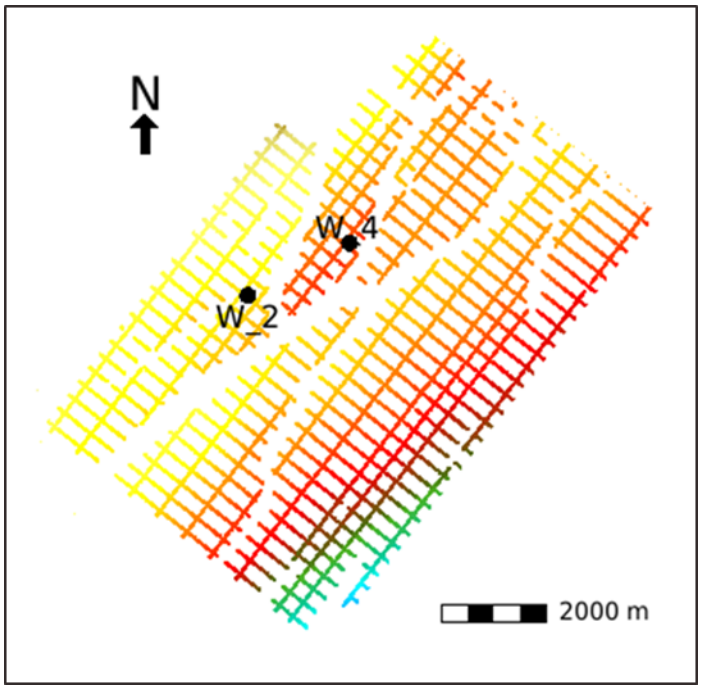

Figure 4.3 Map view for the bottom of Shangmajiagou or the top of Xiamajiagou.

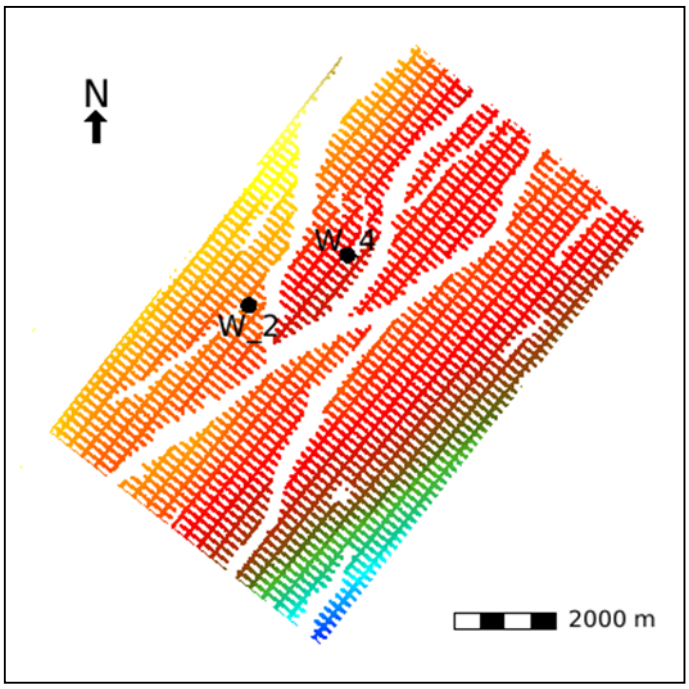

Figure 4.4 Map view for the bottom of Xiamajiagou.

Acoustic impedance is inverted from a 60 Hz high-resolution seismic dataset using post-stack inversion by the constrained sparse spike method. Constrained sparse spike inversion is a trace-based inversion that heavily relies on the seismic information. The limit for post-stack inversion can only generate the compression velocity from the seismic data.

According to the well log analysis in Chapter 3, the reservoir can be identified with an impedance of less than 16500 g/cc*m/s. The inverted acoustic impedance across W2 and W4 respectively shows that the low impedance zones are highly developed at the top of the buried-hill and at the southwest area around the bottom of the Ordovician Formation. Few low impedance zones in the middle of Ordovician formation are

developed (Figure 4.6). The fractured zones and high porosity zones detected from the log curves are characterized by low impedance. The inline and crossline section views across W2 indicate that the fractured zone identified from logs has a low impedance response in the inverted acoustic impedance (Figure 4.7, and Figure 4.8). In addition, the inline and crossline section views across W4 illustrate the high porosity zones and fractured zones which are both characterized by low impedance of less than 16500 g/cc*m/s in the inverted acoustic impedance (Figure 4.9, and Figure 4.10).

Furthermore, when integrating rock physics modeling with seismic inversion, the inverted impedance volume is transformed into the inverted porosity and pore structure parameter product by using the relationship built in Chapter 3 : $\mathrm{AI} = 19000 - 7000(\emptyset \times \gamma)$. The productive reservoir presents a higher porosity and pore structure parameter product. The inverted product across W2 and W4 is shown in Figure 4.11. Both fractured zones and high porosity zones have a higher porosity and pore structure parameter product (Figure 4.12, Figure 4.13, Figure 4.14, and Figure 4.15).

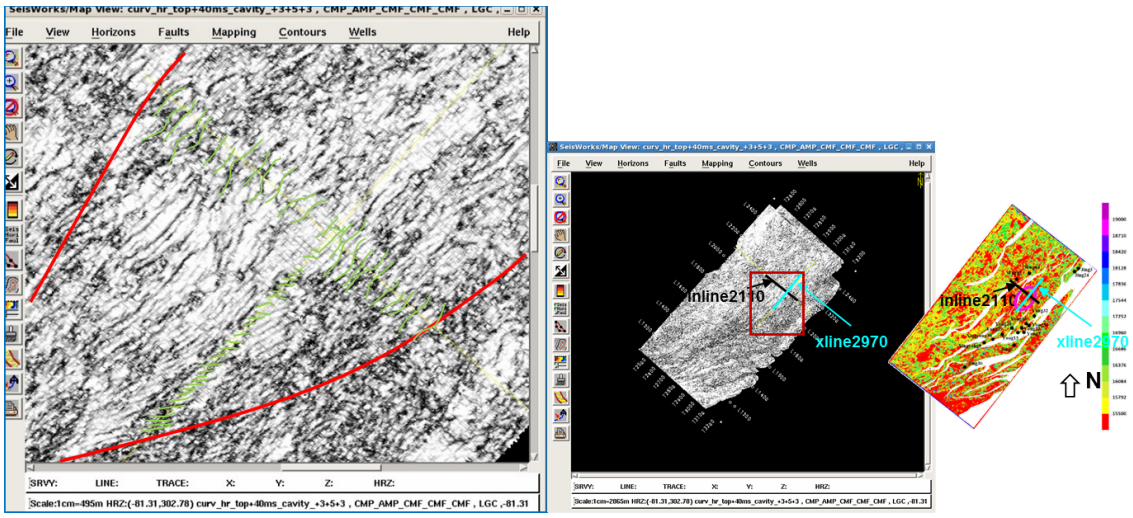

Figure 4.5 Seismic attributes analysis on the most positive curvature in the study area (Li, 2014).

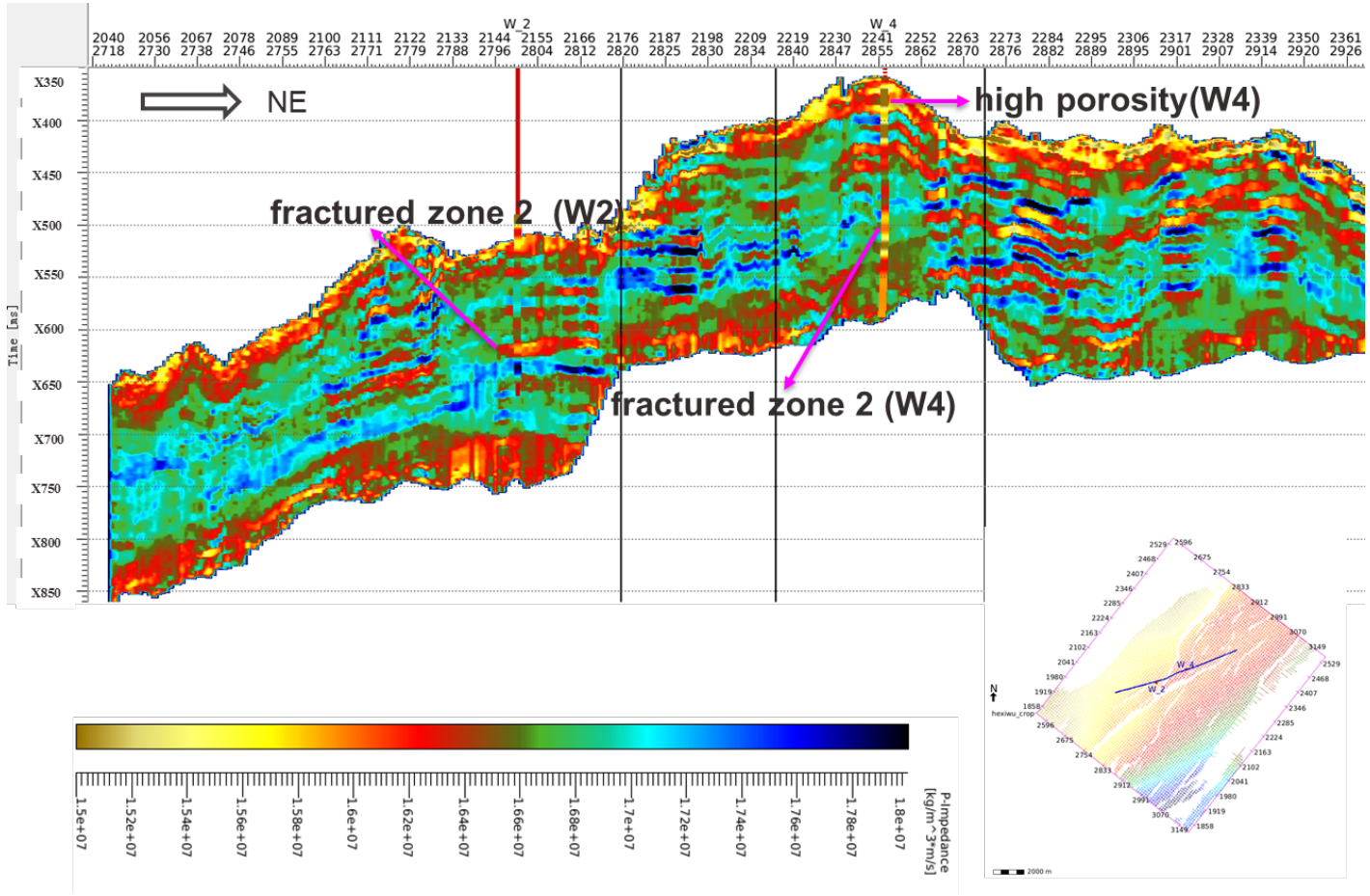

Figure 4.6 Inverted acoustic impedance results section view across W2 and W4. (a) high porosity zone in W4 (b) fractured zone 2 in W2 (c) fractured zone 2 in W4.

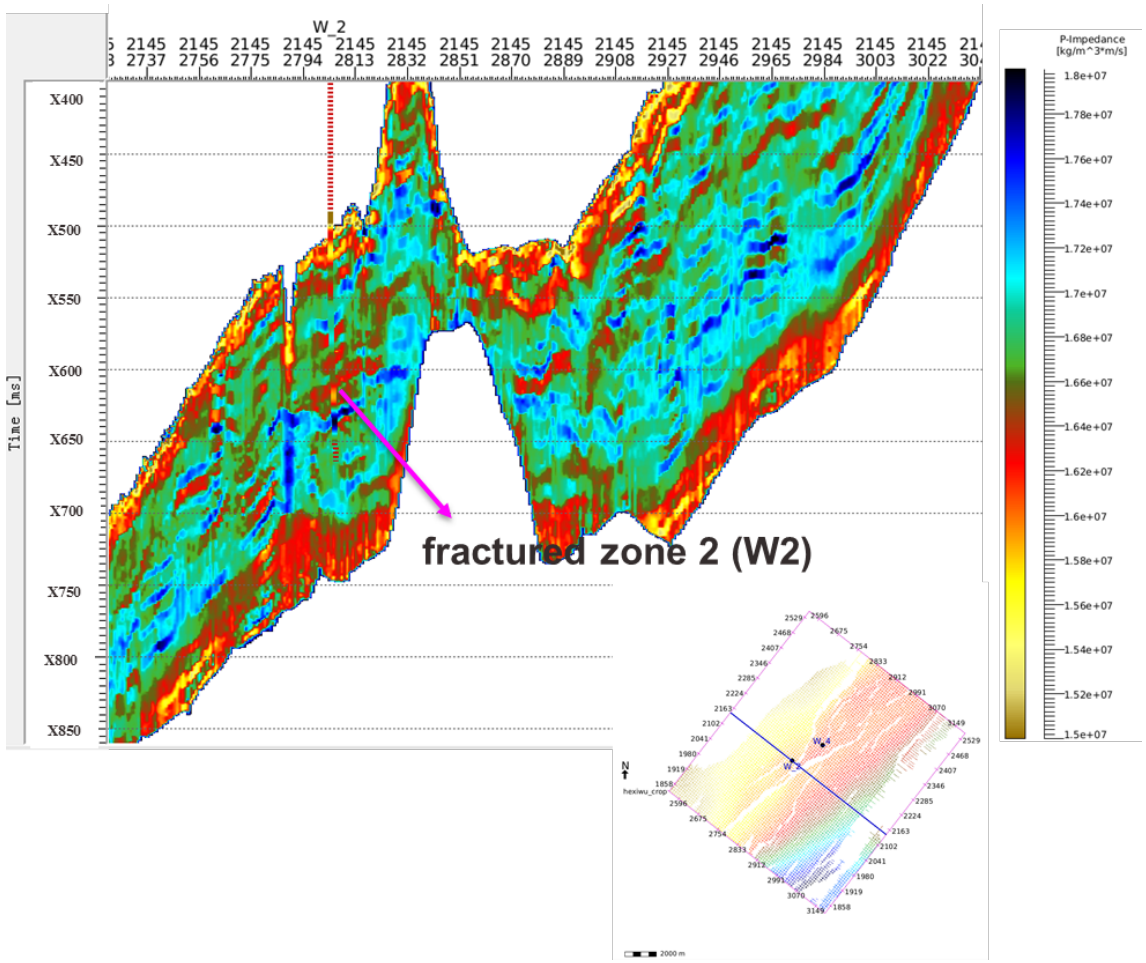

Figure 4.7 Inverted acoustic impedance inline section view across W2.

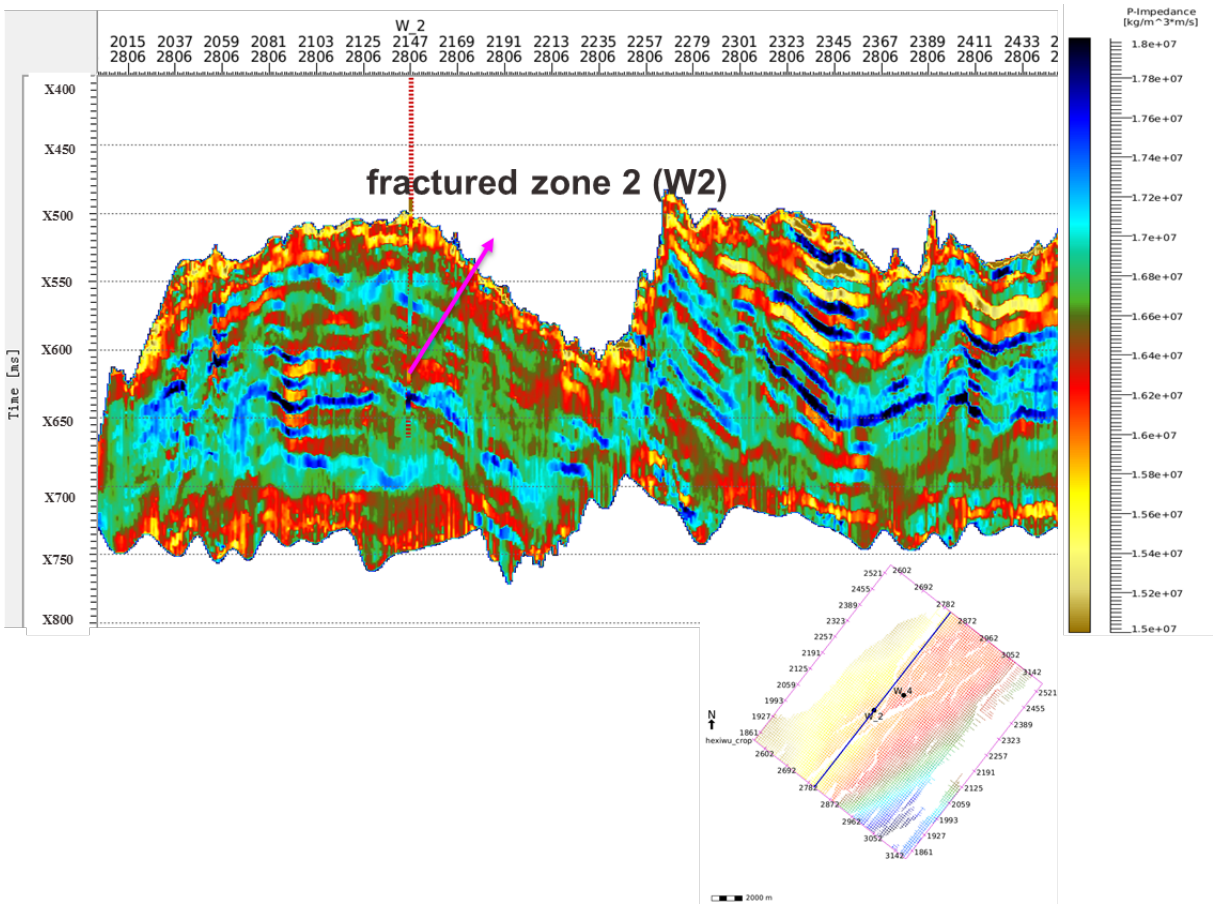

Figure 4.8 Inverted acoustic impedance crossline section view across W2.

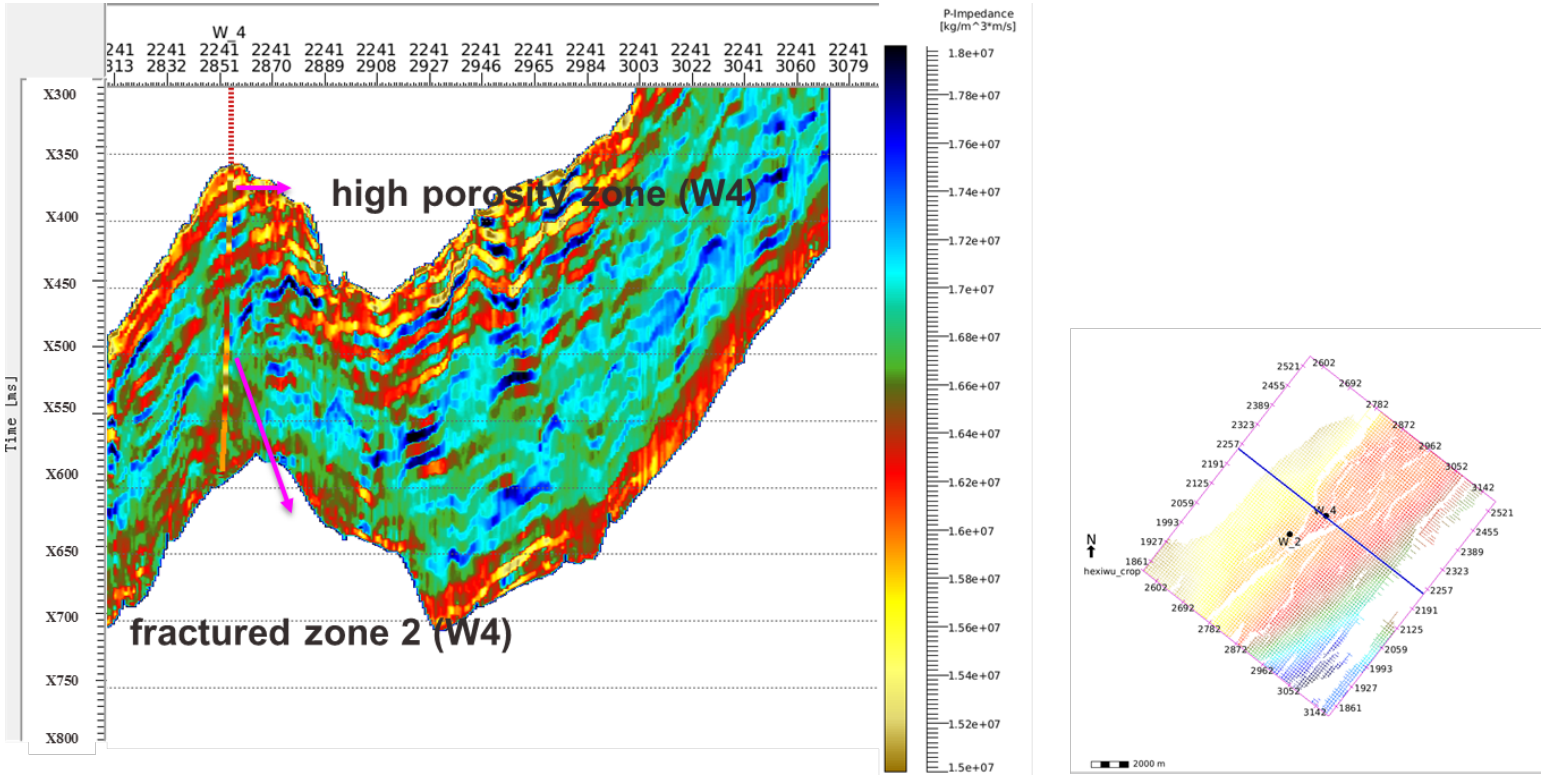

Figure 4.9 Inverted acoustic impedance inline section view across W4.

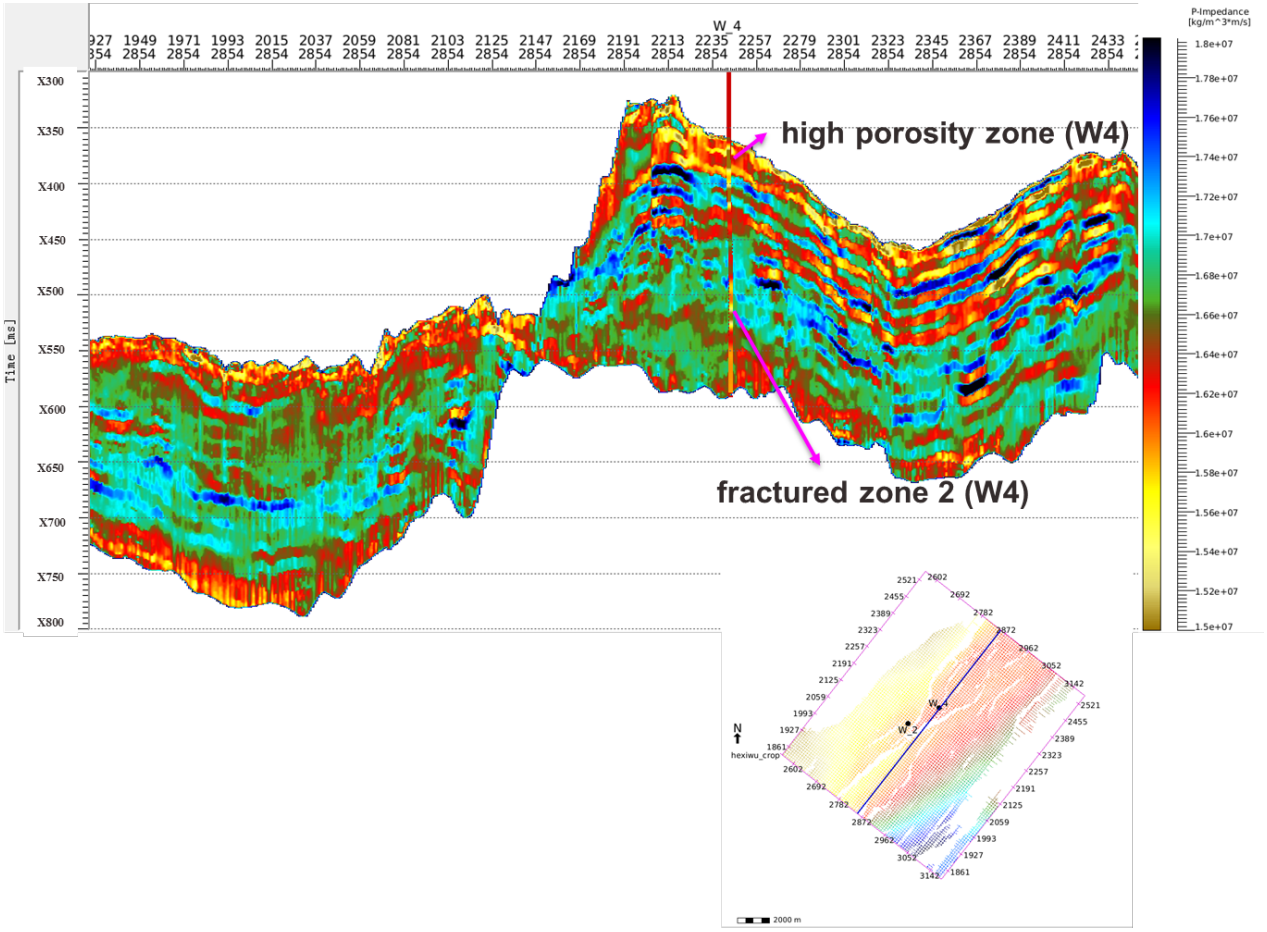

Figure 4.10 Inverted acoustic impedance crossline section view across W4.

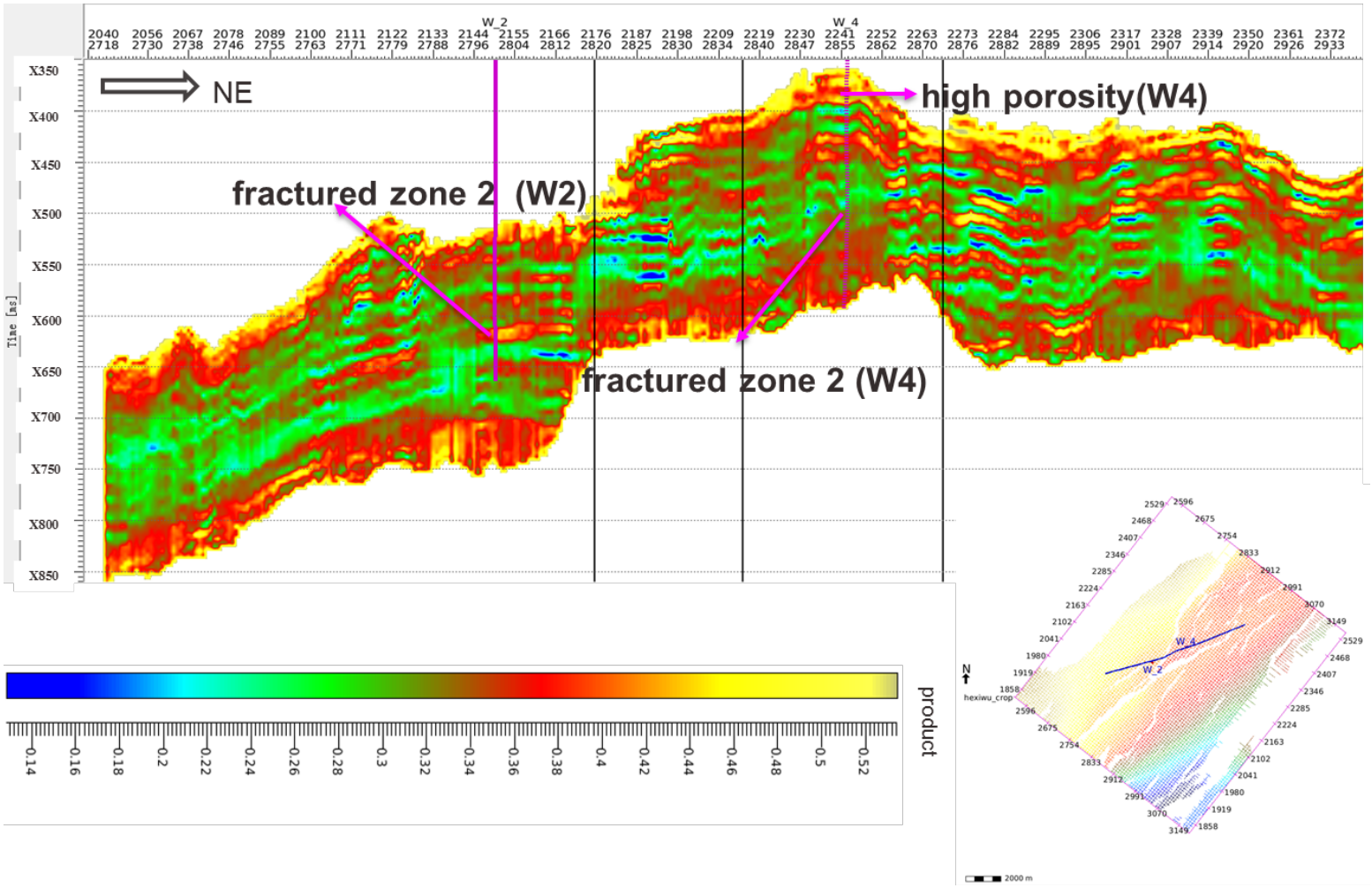

Figure 4.11 Inverted porosity and pore structure parameter product section view across W2 and W4. (a) high porosity zone in W4 (b) fractured zone 2 in W2 (c) fractured zone 2 in W4.

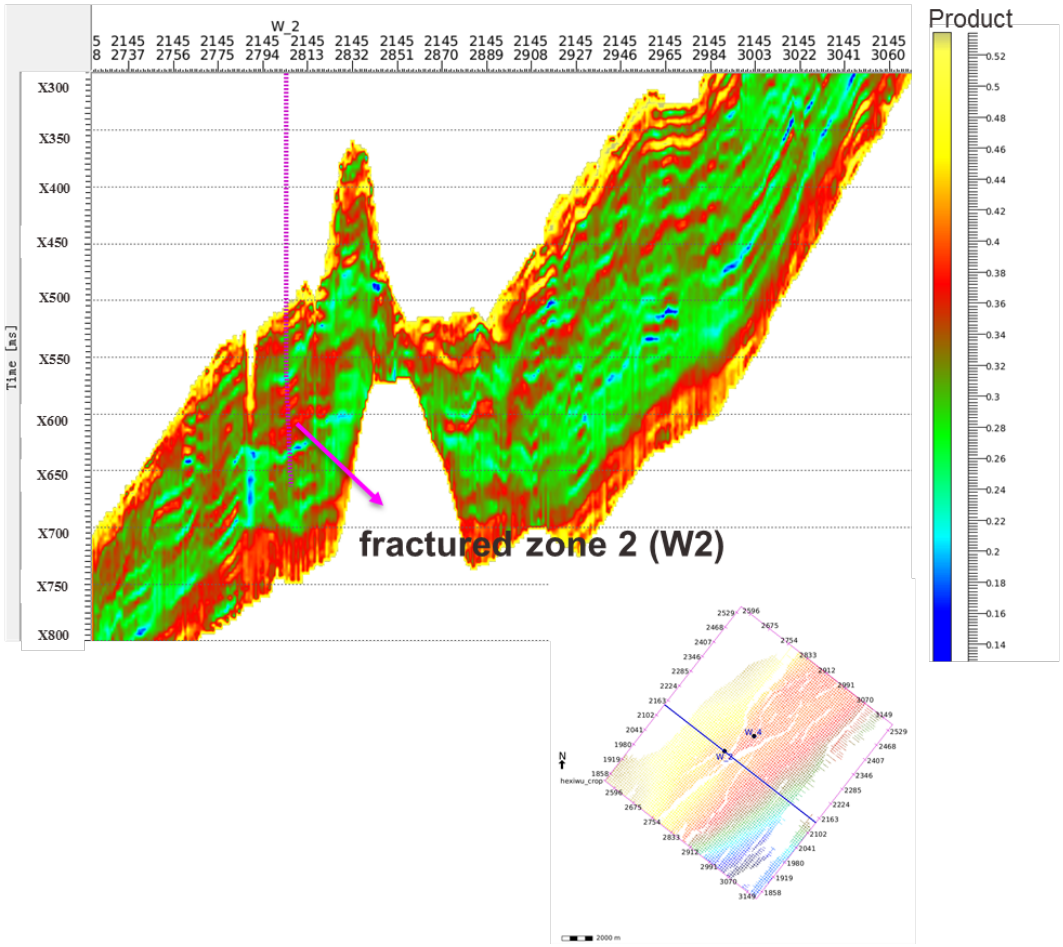

Figure 4.12 Inverted porosity and pore structure parameter product inline section view across W2.

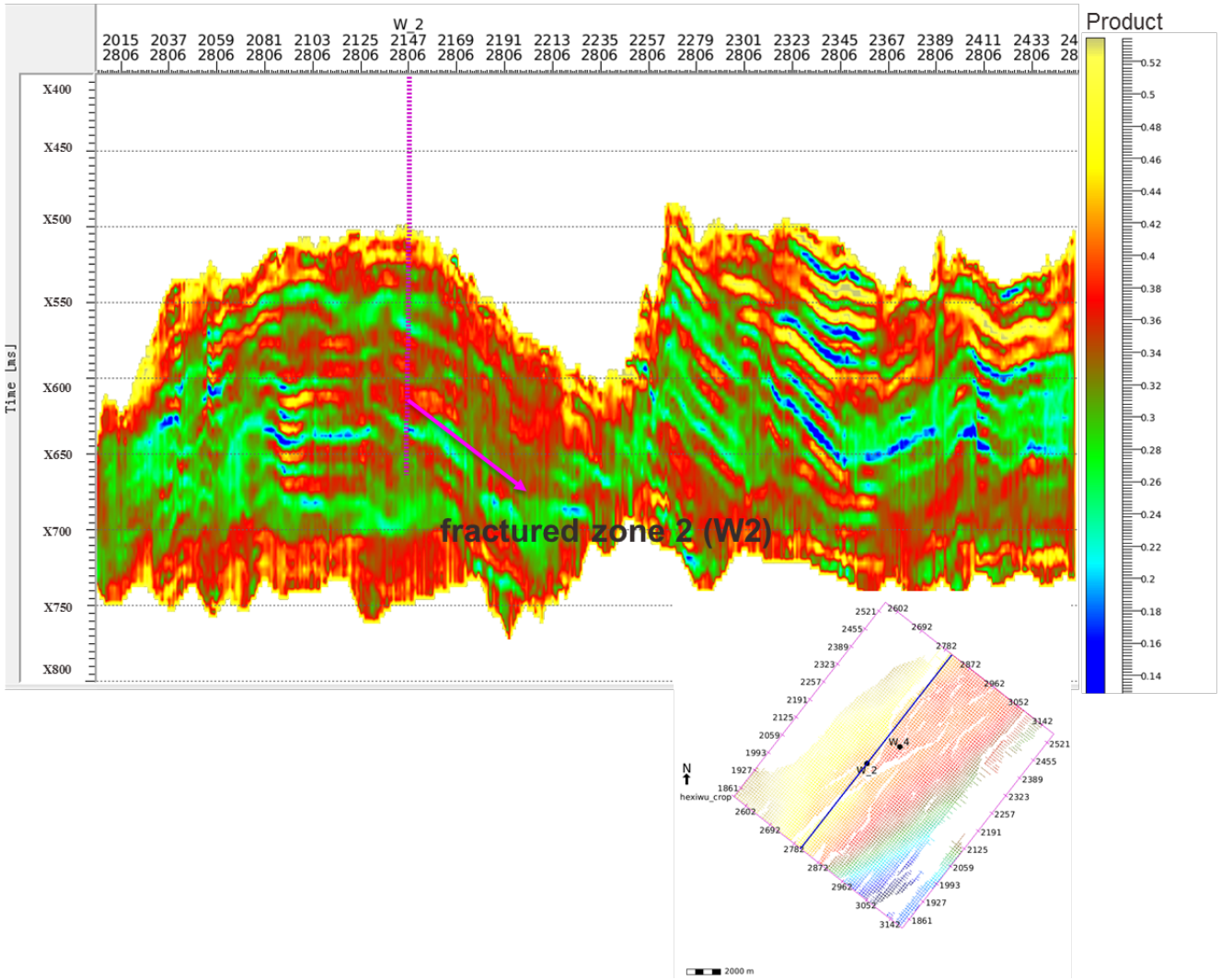

Figure 4.13 Inverted porosity and pore structure parameter product crossline section view across W2.

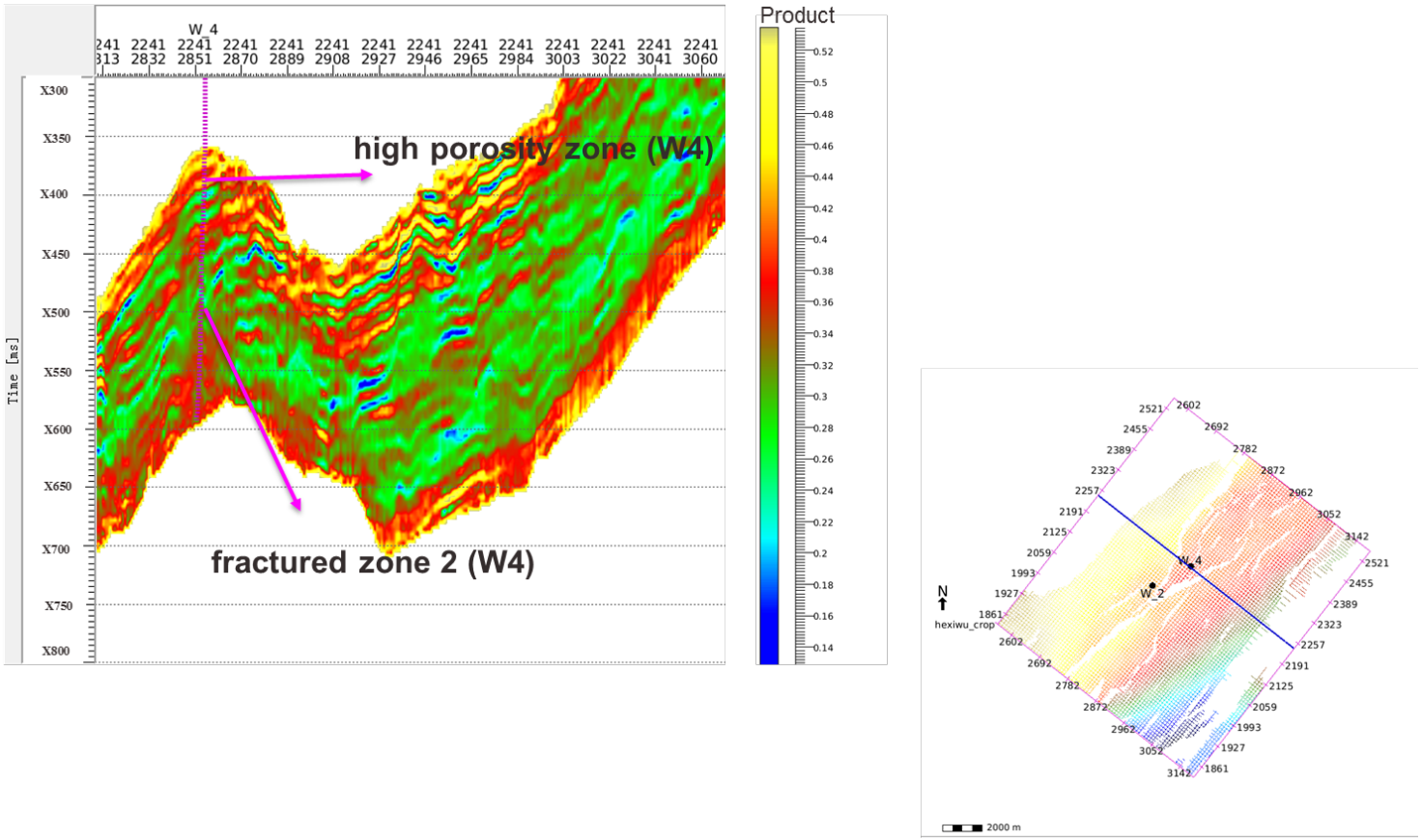

Figure 4.14 Inverted porosity and pore structure parameter product inline section view across W4.

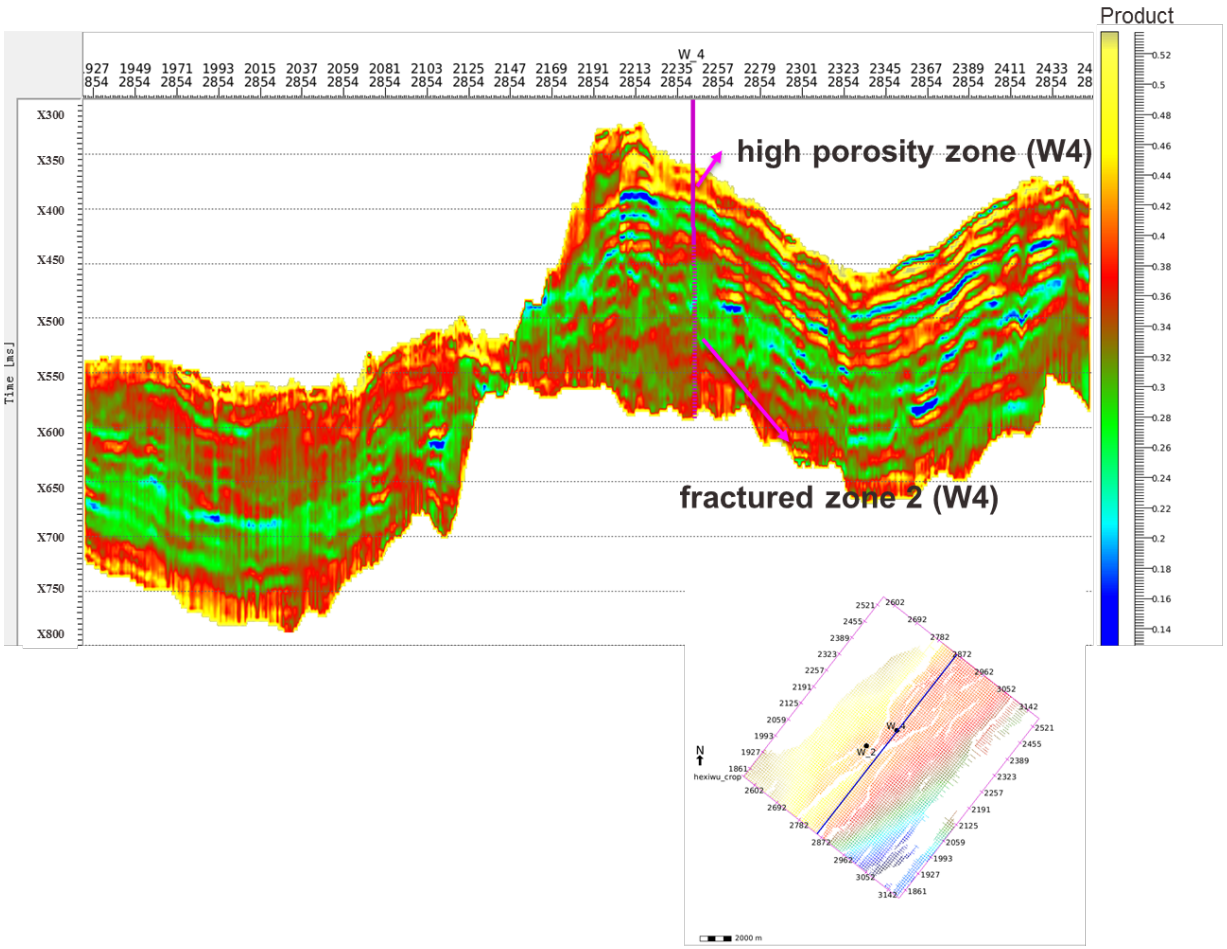

Figure 4.15 Inverted porosity and pore structure parameter product crossline section view across W4.

The timeslice extract from the inverted impedance and inverted porosity and pore structure parameter product along the fractured zone and high porosity zone in W2 and W4 is shown in Figure 4.16 and Figure 4.17. It presents the high porosity zones interpreted from W4 , which are distributed around the top of the buried-hill and are caused by weathering and leaching at the uniformity surface. For the fractured zones, it is mostly along the faults block system in the buried-hill in the middle of the Ordovician Formation.

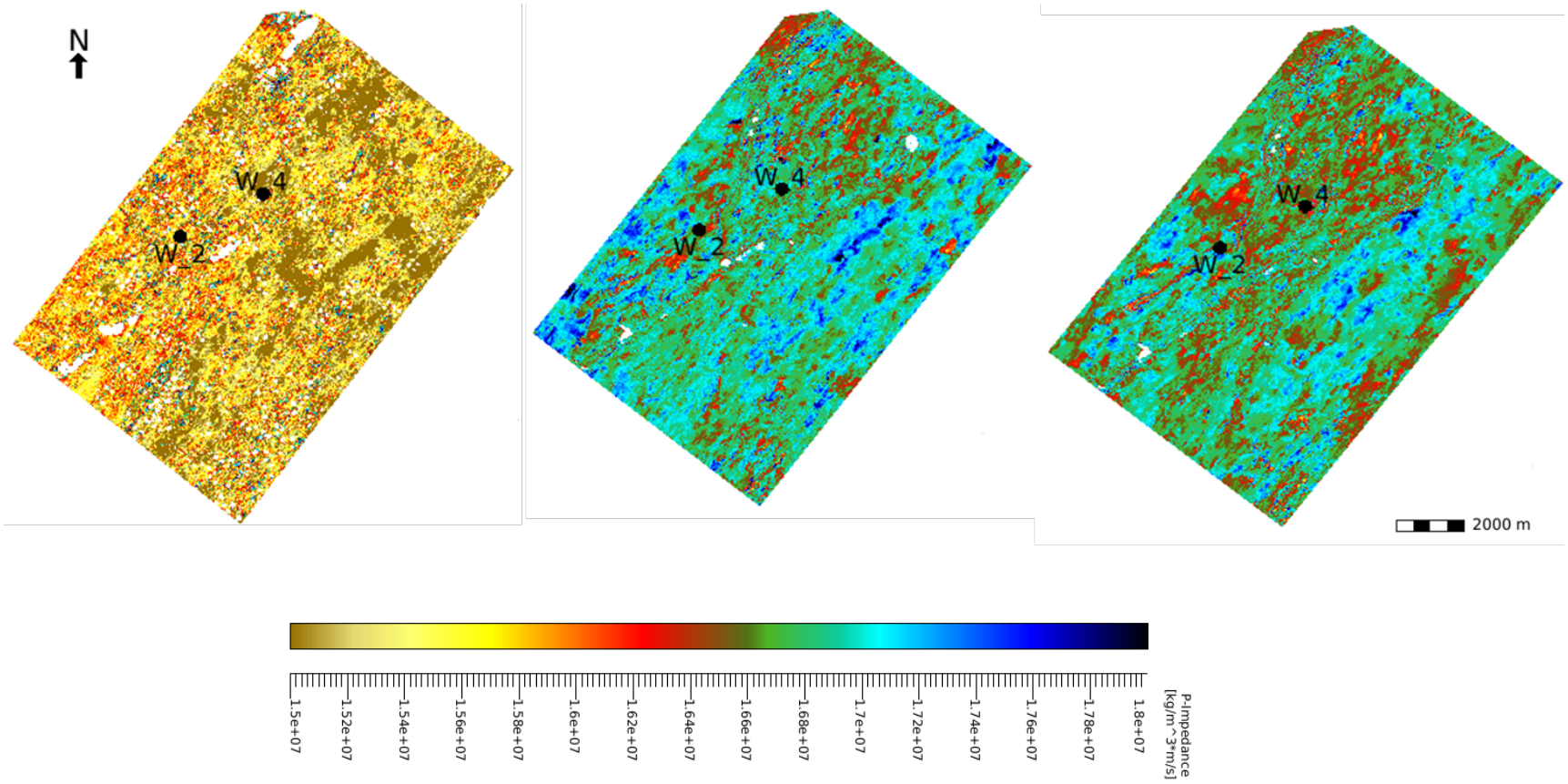

(a) (b) (c)

Figure 4.16 Inverted impedance timeslice (a) high porosity in W4 (b) fractured zone 2 extract along W2 (c) fractured zone 2 extract along W4. a, b and c zones are displayed in Figure 4.6.

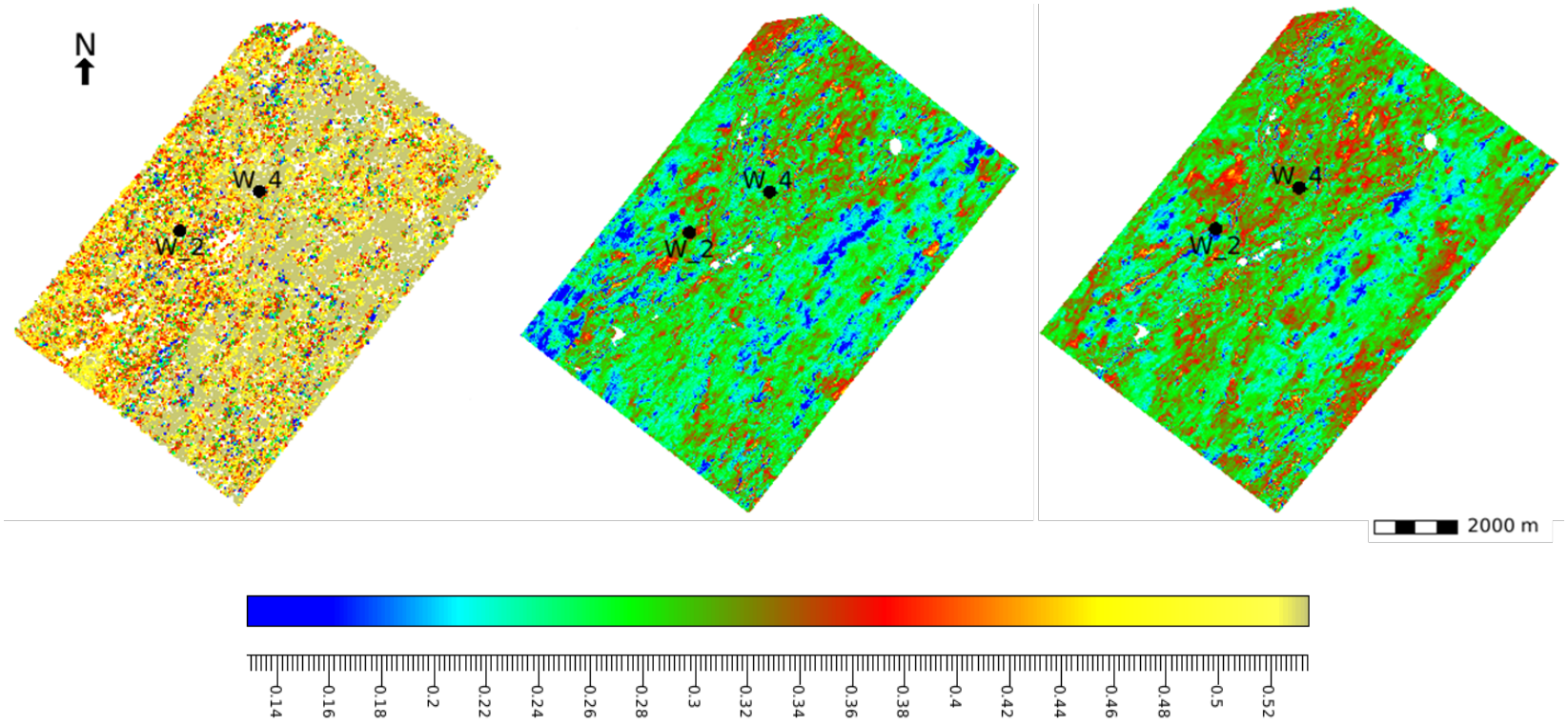

(a) (b) (c)

Figure 4.17 Inverted porosity and frame flexibility factor product timeslice. (a) high porosity in W4 (b) fractured zone 2 extract along W2 (c) fractured zone 2 extract along W4. a, b and c zones are displayed in Figure 4.11.

5. CONCLUSION

The reservoir types in the buried-hill carbonate reservoir of the Ordovician Formation can be identified as high porosity zones (ϕ>6.5%) and fractured zones (ϕ<6.5%) based on well log analysis and rock physics analysis. Fractured zones in the studied reservoirs have an acoustic impedance of lower than 16500 (g/cc*m/s), a bulk modulus of less than 60 GP, and pore structure parameters higher than 14. By applying a rock physics model using the pore structure parameter γ, it is found that acoustic impedance correlates well with the porosity product and this pore structure parameter for the oil reservoir of the ultra-deep carbonate buried-hill of the Ordovician Age. Quantitative geological interpretation indicates that the high porosity zone distributed along the top of the buried-hill is caused by weathering and leaching whereas fractured zones are mostly located along the fault block system.

REFERENCES

Dou, Q., 2011, Rock-physics-based carbonate reservoir pore type evaluation by combining geological, Petrophysical and Seismic data: Ph.D. dissertation, Texas A&M University.

Dou, Q., Y. Sun, and C. Sullivan, 2011, Rock-physics-based carbonate pore type characterization and reservoir permeability heterogeneity evaluation, Upper San Andres reservoir, Permian Basin, West Texas: Journal of Applied Geophysics, **74**, 8-18.

Guo, J., Y. Guo, and L. Wang, 2009, Features of buried-hill reservoirs in Hexiwu structural belt, Langgu Sag, Jizhong Depression: Petroleum Exploration and Development, **36**, 701-708.

Russell, B. H., 1988, Introduction to seismic inversion methods: Society of Exploration Geophysicists.

Sun, Y., 2000, Core-log-seismic integration in hemipelagic marine sediments on the eastern flank of the Juan de Fuca Ridge: Proceedings of the Ocean Drilling Program. Scientific results, Ocean Drilling Program, 21-35.

Sun, Y., and D. Goldberg, 1997, Effects of aspect ratio on wave velocities in fractured rocks: SEG, Expanded Abstracts, 925.

Sun, Y. F., 2004, Pore structure effects on elastic wave propagation in rocks: AVO modelling: Journal of Geophysics and Engineering, 1, 268.

Yi, S., S. Zhao, B. Fan, J. Liu, N. Yang, and H. Xie, 2010, Development characteristics of Buried-Hill and reservoir-forming pattern in central faulted structural belt of

Jizhong Depression: ACTA PETROLEI SINICA (in Chinese with English abstract), v.3, 002.

Zha, Q., 1984, Jizhong Depression, China-its geologic framework, evolutionary history, and distribution of hydrocarbons: AAPG Bulletin, **68**, 983-992.

Zhang, T., Q. Dou, Y. Sun, and H. Zhang, 2012, Improving porosity-velocity relations using carbonate pore types: 2012 SEG Annual Meeting, Society of Exploration Geophysicists.

Zhao, X., F. Jin, Q. Wang, and G. Bai, 2015, Buried-hill play, Jizhong subbasin, Bohai Bay basin: A review and future prospectivity: AAPG Bulletin, **99**, 1-26.